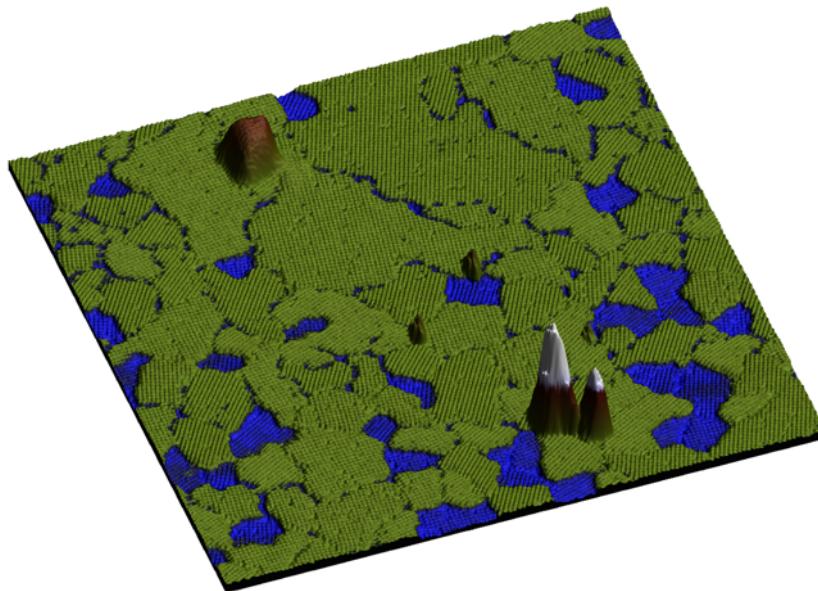


CO₂ sequestration using bacterial surface layers

Master Thesis
University of Twente
October 1st, 2012 – October 1st, 2013

Bart Stel



EPFL

Thesis Director:
Dr. Magali Lingenfelder

Max Planck-EPFL Lab
for Molecular Nanoscience
École Polytechnique Fédérale de
Lausanne

Route Cantonale
1015 Lausanne
Switzerland

University of Twente
Prof. Dr. Frieder Mugele
Physics of Complex Fluids
University of Twente

Prof. Dr. Ir. Harold Zandvliet
Physics of Interfaces and
Nanomaterials
University of Twente

Drienerlolaan 5
7522 NB Enschede
The Netherlands

Abstract

Natures unparalleled way of creating functional nanostructures through self-assembly has inspired the use of biomimetic methods to develop novel processes and materials. An interesting model system is formed by the self-assembly of the SbpA protein (*Lysinibacillus sphaericus* - ATCC 4525, MW 132 kDa) into surface layers (S-layers). Crystalline S-layers are known to mineralize CaCO_3 on their surfaces, a process also responsible for so called 'whiting events' in lakes. Diffusion of CO_2 to solution is the main source of carbon, which therefore identifies this process as a natural way for atmospheric carbon sequestration.

In order to explore the mechanisms of CO_2 sequestration, the formation of CaCO_3 on immobilized crystalline S-layer arrays is analyzed using complementary surface science techniques. Structural information is obtained using Atomic Force Microscopy (AFM) while chemical information is obtained by X-ray Absorption Spectroscopy (XAS). The use of UHV-compatible liquid cells during XAS measurements makes it possible to directly compare the results obtained by in-situ AFM and XAS.

This work shows that the CaCO_3 precipitation pathway on S-layers includes the formation and subsequent stabilization of Amorphous Calcium Carbonate (ACC) versus the thermodynamically most stable polymorph of CaCO_3 – calcite. Furthermore ACC has been found to form and remain stable on S-layers at concentrations far below its known solubility limit. It is therefore concluded that S-layers both catalyze and stabilize the formation of ACC. Moreover, the experimental approach combining in situ XAS and AFM proves to be a powerful method to track biomolecular mechanisms with high spatial and temporal resolution.

Contents

1	Introduction	3
1.1	Bacterial surface layers	4
1.2	Calcium carbonate formation	5
2	Techniques and theory	7
2.1	Atomic Force Microscopy	7
2.1.1	TappingMode	7
2.1.2	PeakForce Tapping	9
2.2	X-ray Absorption Spectroscopy	9
2.2.1	Synchrotron radiation	11
2.2.2	XAS static liquid cell	12
3	Results and Discussion	14
3.1	Ex-vivo S-layer recrystallization	14
3.2	Calcium carbonate precipitation on immobilized S-layers	16
3.3	ACC formation on S-layers investigated by AFM	17
3.4	ACC formation on S-layers investigated by XAS	21
3.5	In-situ tracking of ACC formation on S-layers	27
3.5.1	In-situ AFM	27
3.5.2	In-situ XAS	33
4	Conclusion and outlook	37
4.1	Conclusion	37
4.2	Outlook	37
5	List of presentations	39
6	Acknowledgments	40
A	Directed self-assembly of bacterial surface layer proteins	41
B	Decomposition of ACC under influence of X-ray irradiation	45
C	SbpA purification and S-layer growth protocols	49
C.1	SbpA purification	49
C.2	Ex-vivo S-layer crystallization	54
D	Data analysis of X-ray Absorption spectra	55

1. Introduction

The recent publication of the United Nations' Intergovernmental Panel on Climate Change reporting a 95 percent probability that the global warming is man-made, reinforces the idea that it is of paramount importance to find ways to lower worldwide CO₂ emissions [1]. Research into carbon sequestration processes plays an essential role in this effort.

The capture of atmospheric CO₂ can happen through a multitude of processes ranging from the use of technology to capture gaseous CO₂ directly from flue gasses to the use of agriculture to grow and subsequently store carbon rich crops [2, 3]. Both approaches have some clear benefits. The direct capture of CO₂ from concentrated flue gasses allows for easy capture and storage. The use of self sustainable biological organisms offers parallelization through great numbers and chemical storage of CO₂ in solid form.

Another mechanism of natural carbon sequestration is most spectacularly observed during so called whitening events in various North American lakes and certain marine environments. These events are named after the emergence of a whitish haze in water as a result of massive CaCO₃ formation. Whitings have been studied for decades and strict chemical precipitation rates have been shown to be inadequate to explain the amount of CaCO₃ that is formed [4]. More recently it was shown that whitings coincide with blooms of certain cyanobacteria known to exhibit biomineralization capabilities [5, 6, 7]. This points towards the catalytic ability of bacteria as responsible for the immense amount of CaCO₃ formed during whitings.

Apart from being able to catalyze the formation of CaCO₃ cyanobacteria are among the earliest organisms to evolve on earth. They are known for their exceptional robustness and capability to survive and even thrive in extreme environments. This combination makes them ideal candidates for use in various carbon sequestration schemes. Especially their use as direct capture mechanism in industrial flue gas flows is promising because it combines the benefits of both synthetic and biological carbon sequestration schemes. Massive parallelization can be achieved by growing dense cultures which can then capture CO₂ directly from concentrated flue gasses through biomineralization [8].

In view of this it is important to have a clear understanding of the mechanisms that bacteria use to catalyze the formation of CaCO₃.

Multiple experiments have been performed and a central observation is that cyanobacteria have two different mechanisms of CO₂ capture. One is related to their photosynthetic capabilities and is responsible for transforming CO₂ into organic compounds, the other involves the inorganic transformation of CO₂ and calcium into CaCO₃ at the surface of the bacterium [9, 6, 7].

Previous studies indicate that the inorganic formation of CaCO₃ at the outer

surface of bacteria might be related to the whitening events [7, 6]. The process might be catalyzed by the protein surface layer – or S-layer – which is crystalline in nature and forms the outermost membrane of many of these bacteria [7, 9, 10]. Therefore a comprehensive understanding of calcium carbonate mineralization in the presence of S-layers is required.

In order to distinguish between internal cellular processes and surface mediated inorganic mechanisms involved in the biomineralization on cyanobacteria, it would be beneficial to separate the two entirely. By using the impressive self-assembling capabilities of the proteins that make up the outermost surface, S-layers can be recrystallized ex-vivo where they form two dimensional crystalline sheets that can be immobilized on the surface of various substrates [10, 11, 12, 13].

Here I present the study of carbon mineralization at the interface of bacterial surface layers ex-vivo. The S-layers used in this study are recrystallized from SbpA proteins of the *Lysinibacillus sphaericus* species. These bacteria have been shown to catalyze the formation of CaCO_3 [14, 9].

To obtain both structural as well as chemical information about the process, in-situ Atomic Force Microscopy (AFM) is combined with in-situ X-ray Absorption Spectroscopy (XAS) at the solid-liquid interface.

1.1 Bacterial surface layers

Due to the central role of bacterial surface layers in this research I will give a more thorough description of S-layers in this section.

As mentioned in the introduction, S-layers make up the outermost cell membrane of many bacteria and almost all archaea. The layers are composed of individual proteins (SbpA) which self-assemble into regularly ordered lattices with natural occurring symmetries ranging from oblique (p1, p2), square (p4) to hexagonal (p3, p6) [15]. The unit cells of these layers range in size from 3 to 30 nm, depending on the organism [11]. See figure 1.1.

In case of the *Lysinibacillus Sphaericus* the unit cell is composed of four individual monomers which results in a square symmetry of the resulting layer. The formation of S-layers is multi-step process, only when four monomers have formed a tetrameric unit cell they can start to self-assemble into crystalline layers [16, 12]. The limiting step in the formation of S-layers is the completion of the tetramer. Therefore the most common defect that is observed in S-layers is the incorporation of incomplete tetramers.

The individual SbpA proteins can be purified by exposure of S-layers to high concentrations of chaotropic agents like guanidine hydrochloride after which the monomers can be collected by membrane diffusion [15]. Recrystallization can be triggered by exposure to Ca^{2+} which acts like a cross linker between individual monomers. Based on the concentration of monomers in solution the S-layers can form free floating sheets in solution or form an immobilized monolayer on the surface. Throughout the experiments described in this thesis an SbpA protein from the *Lysinibacillus sphaericus* (ATCC 4525, Molecular Weight of 132 kDa) is used, which is known to reliably form S-layers with

square symmetry [12].

For the complete SbpA purification and S-layer recrystallization protocols see appendix C.

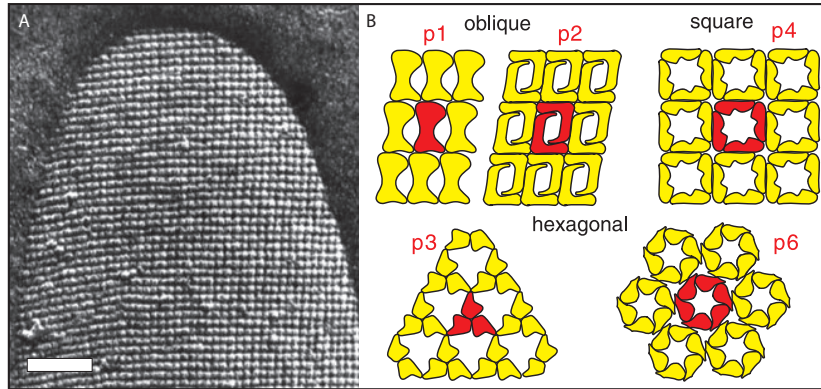


Figure 1.1: Overview of the different geometries of naturally occurring S-layers.

(A) Electron micrograph of a micro-organism exhibiting a square S-layer lattice. The scale bar corresponds to 100 nm.

(B) A schematic drawing showing the various S-layer lattice symmetries observed in nature (Figure 1 from Sleytr et al. [15, 17]).

1.2 Calcium carbonate formation

Calcium carbonate plays a significant role in the biosphere, numerous organisms use CaCO_3 in their shells, skeletons and other useful biominerals.

Despite its relevance and over a century of research into the topic, the nucleation pathways that lead to CaCO_3 are not fully understood.

In literature two mechanisms are described. In the classical picture dissolved ions form clusters which only after passing a critical size will grow into larger crystals through diffusion of particles to the surface of existing nuclei and incorporation in the crystal lattice [18]. Growth experiments of CaCO_3 on Self-Assembled Monolayers (SAMs) are in agreement with this mechanism. While the formation of ACC and calcite has been observed simultaneously, over time the ACC dissolves in favor of calcite growth [19].

Other experimental observations however suggest that the nucleation and subsequent crystallization process of CaCO_3 follows a more complex nucleation pathway involving the formation of stable prenucleation particles that can exist in solution even well below saturation levels [20, 21]. Recent molecular dynamics simulations hint to the possibility that these prenucleation particles are in fact a dense liquid which after solidification form amorphous calcium carbonate particles [22].

Studies on biogenic CaCO_3 formation on sea urchin spicules have shown that the amorphous polymorph acts as a precursor to more ordered crystalline structures. A transition from ACC to calcite has been shown to go through an intermediate 'dehydrated ACC' phase [23, 24]. Also the transformation and subsequent stabi-

lization of aragonite-like CaCO_3 on the surface of live cyanobacteria is reported [5, 25].

Multiple processes have been reported experimentally, however no complete mechanism for CaCO_3 formation has been proposed that can explain the various observations.

By growing S-layers ex-vivo, the inorganic CaCO_3 formation can be studied isolated from other processes, this could give a valuable new point of view on this topic. Furthermore the initial formation and subsequent transition of ACC could be followed right from the start with high temporal and spacial resolution by AFM and XAS.

For comparability with studies done in natural environments, the in-situ formation of CaCO_3 is designed to closely mimic the conditions present in the lakes where also whitening events have been observed. CaCl_2 and NaHCO_3 concentrations that are used for the formation of CaCO_3 are 10 mM and 3.2 mM respectively [7]. Also a concentration well below the nucleation point of CaCO_3 ¹ (3.5 mM and 3.5 mM respectively) and one well above this point (50 mM and 50 mM) have been used as comparison.

In nature the formation of CaCO_3 starts with the dissolution of CO_2 into water according to equation 1.1. From there the now dissolved CO_2 reacts through several steps with water to end up as carbonate ions. Finally these carbonate ions can react with calcium which is naturally present in lakes to form CaCO_3 , see also equations 1.2 to 1.5 [26].

$$\frac{P_{\text{CO}_2}}{[\text{CO}_2]} = k_H = 29.76 \frac{\text{atm}}{\text{mol/L}} @25^\circ\text{C} \quad (\text{Henry constant}) \quad (1.1)$$

The amount of dissolved CO_2 depends on the partial pressure of CO_2 in the atmosphere and is governed by the constant k_H – the Henry constant [26].



Dissolved CO_2 reacts with H_2O to form CO_3^{2-} through intermediates of H_2CO_3 and HCO_3^- . CO_3^{2-} then combines with Ca^{2+} to form CaCO_3 [26].

¹The nucleation point for CaCO_3 in solution is informed to be reached at 13 mM equimolar concentration of CaCl_2 and NaHCO_3 , [19]

2. Techniques and theory

To characterize the S-layers and their biomineralization properties we use in-situ Atomic Force Microscopy (AFM) and X-ray Absorption Spectroscopy (XAS). AFM is used to obtain structural information of the S-layers and their biomineralization products on the nm scale while XAS is used to probe the coordination chemistry of the CaCO_3 structures in order to distinguish between the various polymorphs of calcium carbonate.

In this chapter I present a compact theoretical basis for these techniques.

2.1 Atomic Force Microscopy

The main working principle of an Atomic Force Microscope relies on the bending of a micrometer sized cantilever when it interacts with the surface of the sample to be measured through a very sharp tip. The bending of the cantilever is directly proportional to the interaction strength with the surface [27].

In order to follow the topography of the sample the bending of the cantilever is registered by measuring the angle at which a laser is reflected off of the reflective backside of this cantilever. This signal is then processed and used as feedback signal to maintain a constant tip-sample separation distance.

While AFM has been around for decades, the limits of the system are continuously pushed forward [27, 28, 29].

The images obtained by AFM shown in this thesis are created using either TappingMode or PeakForce Tapping measurement schemes [28]. Their respective benefits and drawbacks are discussed in the next two paragraphs.

2.1.1 TappingMode

TappingMode AFM has been developed as solution to the various problems with contact mode measurements where the tip is in constant contact with the sample during scanning. In particular the unavoidable shear force between tip and sample can result in sample damage and tip wear.

In TappingMode AFM the tip is brought in resonance by a small piezo, where this resonance frequency can range from several kHz to the MHz range depending on the cantilever characteristics. The cantilever with tip can be modeled as a simple spring-mass system with a resonance frequency $\omega^2 = \frac{k}{m}$. Here the tip-sample interaction acts so as to change the effective mass of the the system and therefore modifies the resonance frequency as well. By keeping the resonance

fixed within a feedback loop, it is possible to maintain a constant tip-sample separation.

Since the tip only interacts with the surface of the sample intermittently, there is hardly any lateral force acting on the tip or sample. This greatly reduces tip wear and enhances sample stability of especially soft samples.

The strength of TappingMode AFM lies in the fact that very high scan speeds can be maintained while minimizing the shear force acting on the sample. From high speed measurements done in TappingMode on the FastScan system scanning speeds up to $800 \mu\text{m/s}$ have been achieved while maintaining reasonable surface tracking.

To understand the main limitation of TappingMode AFM one can have a look at figure 2.1. In 2.1(i) a plot of Force versus time is shown, where the blue and red line represent the approaching and retracting part respectively. During the course of one cycle of approach and subsequent withdraw there are acting different forces on the tip. At point (B) there is a jump-to-contact due to an instability caused by the non-linear Van der Waals force overcoming the linear spring force of the tip. At point (C) the tip is pushed against the surface which results in a repulsive force due to the short range Coulomb interaction between tip and sample. And at point (D) forces caused by Van der Waals forces, and capillary forces (only in air) result in a strong adhesive force. Since all these forces act on the tip within one period of the oscillation, only their summed contribution is taken into account when the resonance frequency is used as feedback signal and individual force feedback is impossible.

This is also the reason why the most sensitive TappingMode measurements, i.e. on soft materials, are usually done in-situ with Peak Forces kept as low as possible. The aqueous environment greatly reduces the adhesion forces and the

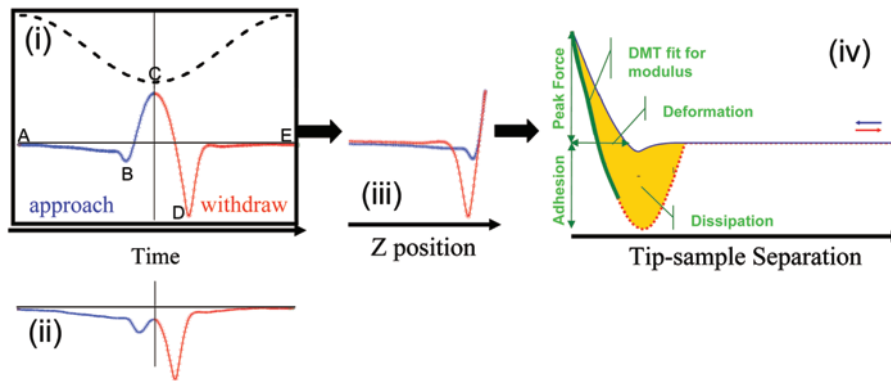


Figure 2.1: The probe motion during AFM TappingMode schematically displayed. (i) Force (red-blue line) and piezo Z-position (black dashed line) versus time. In chronological order: Start (A), the jump-to-contact point (B), maximum applied force – Peak Force (C), maximum adhesion force (D), end (E). (ii) Same as (i) however now with small Peak Force. (iii) Eliminating the time variable results in a plot of Force versus Z piezo position. (iv) Plot of Force versus Separation distance between tip and sample. From this various sample features like adhesion, deformation and dissipation can be extracted. (Figure 1 from Pittenger et al. [28]).

low PeakForce reduces the sample deformation significantly. Since the environment and tip depending features are thus reduced, the relative contribution of tip-sample interactions to the total force is increased.

2.1.2 PeakForce Tapping

A different approach which tries to overcome the inherent limitations of TappingMode AFM is the newly developed PeakForce Tapping mode [28]. In this approach the cantilever is oscillated at a frequency up to 8 kHz, i.e. well below resonance. For every oscillation cycle the complete force vs. time signal is extracted. This makes it possible to isolate the peak force – point C in figure 2.1(i) – every time the tip interacts with the sample. With this information the Peak Force can be used as feedback signal and this enables a constant peak force independent of adhesion forces that act on the tip.

A drawback of this method is the reduced acquisition time due to the large amount of data that is collected and the requirement of real time processing.

2.2 X-ray Absorption Spectroscopy

The XAS measurements presented in this thesis were performed at the Advanced Light Source (ALS) in Berkeley, in collaboration with the group of Dr. Jinhua Guo.

The energy of X-rays lies in the range of 500 eV to 500 keV. Upon interaction with an atom these photons have enough energy to excite core-level electrons. The result is that the X-ray is absorbed, the core-level electron is excited into vacuum and the absorbing atom is left with an unoccupied core energy-level.

This excited state can decay using one of two possible mechanisms, through X-ray fluorescence or through the Auger effect 2.2.

During X-ray fluorescence the hole in the core-level created by the absorption event is filled by an electron from a higher energy level within the same atom. By moving to a lower level the electron is left with excess energy, which is emitted in the form of an X-ray photon. The energy difference between these two levels is characteristic of the atom, therefore the X-rays that are emitted this way can be used to identify the chemical state of the absorbing atom.

During the Auger effect the core-level hole is again filled by an electron from a higher energy level within the same atom. However unlike X-ray fluorescence, the excess energy is now transferred to yet another electron which is subsequently emitted from the atom.

Both processes are directly proportional to the absorption probability and the total amount of either X-ray photons or Auger electrons is a measure of the absorption probability.

X-ray Absorption Spectroscopy (XAS) – or X-ray Absorption Fine Structure (XAFS) – is based on the absorption of X-rays as described above. The XAFS can be divided into two parts, the X-ray Absorption Near-Edge Spectroscopy (XANES) and the Extended X-ray Absorption Fine-structure Spectroscopy (EXAFS) [30]. Here XANES is the part of the XAFS spectrum within $\sim 50\text{eV}$ of the absorption edge, whereas everything beyond that falls under the EXAFS region.

Both XANES and EXAFS are based on the same physical process and their distinction is primarily made for convenience for interpretation. The XANES part of the spectrum is most sensitive to the oxidation state and coordination chemistry of the absorbing atom. Oscillations in the EXAFS signal due to constructive and destructive interference of neighboring atoms make this part off the XAFS spectrum more sensitive to the distances, coordination number and species of the neighbors of the absorbing atoms.

One of the main attractions of XAFS is that it can be used to study non-crystalline materials as well as crystalline, regardless of the physical form of the sample [31].

The reason why XAFS is such a powerful measurement tool can be found in the absorption coefficient, given in equation 2.1.

$$\mu \approx \frac{\rho Z^4}{AE^3} \quad (2.1)$$

Here μ is the absorption coefficient which determines the absorption probability, ρ is the sample density, Z is the atomic number, A is the atomic mass and E is the X-ray energy.

The absorption coefficient depends strongly on both the atomic number as well as the X-ray energy and this is the reason that by tuning the X-ray energy one can achieve good contrast between different materials [31].

The interpretation of the XANES spectrum can be difficult due to the lack of a simple analytic or physical description. It is however not always necessary to explain the numerous features of the XANES spectra. Often it is sufficient to compare the shape of the XANES spectrum with references from known materials so as to identify the compounds within the sample [32].

This ‘fingerprinting’ provides a straightforward analysis method which in combination with the high sensitivity of XANES for the coordination chemistry makes X-ray absorption spectroscopy a suitable method to obtain chemical information of CaCO_3 on top of S-layers, ex-situ as well as in-situ.

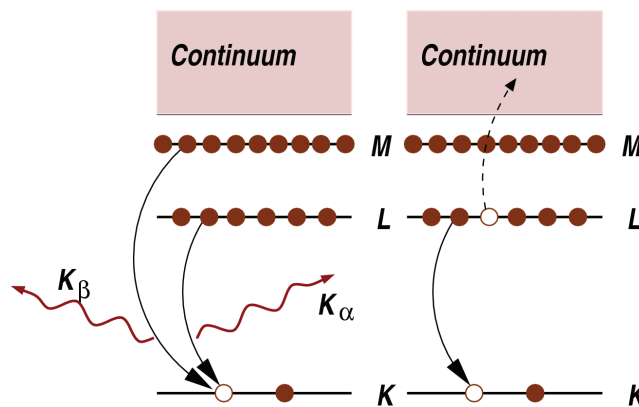


Figure 2.2: Schematic representation of the two mechanisms through which the excited state can decay. X-ray fluorescence on the left, emission of electrons due to the Auger effect on the right. The probability of both mechanisms is directly proportional to the absorption probability of the X-ray photon (Figure 2.5 from Newville [31]).

2.2.1 Synchrotron radiation

In order to measure the full XANES spectrum a tunable high-intensity X-ray source is required. Such a tunable X-ray beam can be produced at a synchrotron radiation source [33, 34].

Here electrons are accelerated in a circular pattern to relativistic speeds. According to the Maxwell equations, charged particles will radiate energy when accelerated, i.e. when their direction is changed [35]. At non-relativistic speeds, the radiation pattern resembles a doughnut shaped centered around the particle with its axis towards the center of revolution. However when the particles are accelerated towards relativistic speeds this pattern is distorted due to the Lorentz contraction of space-time, resulting in a narrow cone in the direction of movement of the particle [36, 37]. This X-ray radiation is called synchrotron radiation.

The electrons are confined to a circular pattern by bending and focusing magnets. Only at the bending magnets is the direction of the electrons changed and will they emit radiation.

Over time some electrons will escape the confinement imposed by the focusing magnets, resulting in a decay of radiation that is produced at the bending magnet site. This is counteracted by the injection of bunches of pre-accelerated electrons at precisely timed intervals, so called buckets.

The result is a beam of X-ray radiation at nearly constant intensity smoothly distributed over an energy range which depends on the bending magnet [38].

At the level of the individual beam lines the synchrotron radiation is first diffracted using a tunable monochromator which selects a specific energy by rotating the grating to obtain a specific angle with respect to the incident beam. From here the now monochromatic X-ray beam is focused using beamline specific X-ray optics which direct the beam through a pinhole towards the sample to be measured.

The absorption by the sample can be obtained in both transmission and reflection setups.

The X-ray absorption in the sample generates fluorescent photon signal and an Auger electron signal through the mechanisms described before [39, 40].

The Auger effect emits electrons from the sample as a result of absorption of an X-ray photon, leaving the sample in a charged state which in turn creates a potential difference between sample and its surroundings. By connecting the sample to the ground, the current along this potential can be measured. This signal is called the Total Electron Yield or TEY.

The fluorescent signal consists of photons and is measured using a continuous channel electron multiplier, which is more frequently called Channeltron. It multiplies an incoming charge by means of secondary electron emission. The inside of a small glass tube is coated with a semiconducting metallic oxide coating. When an electron strikes this surface with enough energy, it will dislodge on average multiple secondary electrons. By applying a transverse electric field, the electrons will follow a zigzag pattern resulting in an avalanche of outgoing electrons [41]. The same multiplication principle can be applied to incoming photons when a photo-emissive surface is placed in front of the Channeltron.

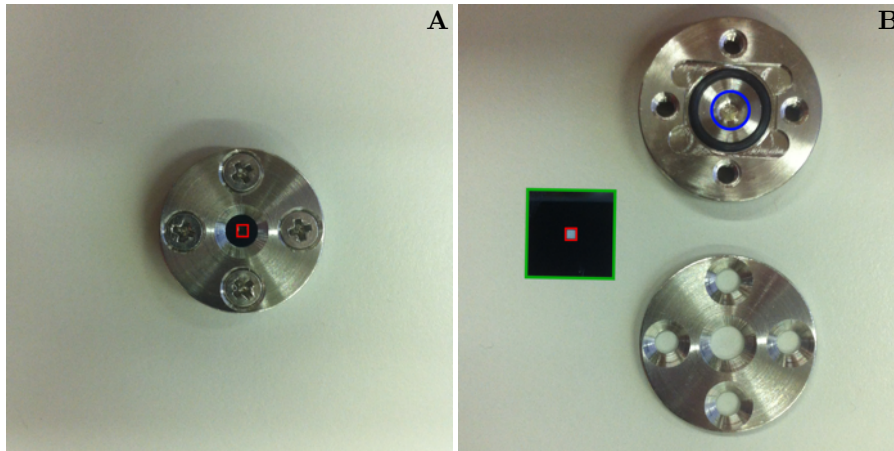


Figure 2.3: Here the in-situ static liquid cell is displayed in both closed (A) and opened (B) configuration. The red square marks the optically transparent 100 nm thin Si_3N_4 window in the middle of the larger $1\text{ cm} \times 1\text{ cm}$ silicon surface, marked in green. The blue circle marks the hollow spacing where the liquid is confined. The four screws in (A) press the cover onto the silicon surface which is therefore sealed against the o-ring.

Difficulties arise when the source emits both photons as well as electrons, as is the case in XAS. The Channeltron cannot distinguish between electron generated by a photon striking the photo-emissive surface or electrons emitted directly from the source. To select only the fluorescent signal one can place a charged grid in front of the Channeltron. By setting the charge of this grid above the energy of the incoming X-ray photons, one can repel the Auger electrons without affecting the uncharged fluorescent photons.

While both TFY and TEY signals are directly proportional to the X-ray absorption probability, they are not entirely interchangeable. Due to the fact that electrons have a much smaller penetration depth in solids compared to photons, the TEY signal has a higher surface sensitivity than the TFY signal.

2.2.2 XAS static liquid cell

In order to measure X-ray absorption spectra from in-situ samples under UHV conditions a barrier between liquid and UHV that is transparent for X-ray photons is required. A 100 nm thin Si_3N_4 surface is both strong enough to withstand the immense pressure difference and optically transparent to X-rays [42, 43]. The implementation of such a Si_3N_4 barrier into a working liquid cell is shown in figure 2.3. The liquid is placed in a hollow spacing which can be sealed off by a $1\text{ cm} \times 1\text{ cm}$ slice of silicon which is pressed against an o-ring. In the middle there is a $1\text{ mm} \times 1\text{ mm}$ Si_3N_4 ‘window’ where the thickness is reduced to 100 nm.

When the X-ray absorption spectrum is recorded using an in-situ static liquid cell, several things change compared to ex-situ measurements. Most important is the presence of a barrier between the sample and liquid on one side and UHV conditions and X-ray beam on the other side.

X-ray photons are able to pass through this optically transparent window and excite atoms on the liquid-side. From there the generated photons or electrons have to travel back through the window in order to reach the Channeltron in the case of photons or simple leave the grounded sample in the case of electrons.

Though necessary for the confinement of a liquid environment, a Si_3N_4 barrier significantly affects the collection of both TEY and TFY. The ability of photons to pass through a certain material depends on both material properties as well as the photon energy and is expressed through the attenuation length – the distance into the material where $\sim 63\%$ of the photons have been absorbed. From equation 2.2 the attenuation for a 100 nm Si_3N_4 barrier can be calculated. Generated fluorescent photons have to pass back through the same barrier which doubles the effective attenuation length. The amount of X-ray photons at 350 eV that is not absorbed by a 100 nm Si_3N_4 barrier 5 %, or 20 times less than in the case without barrier. From figure 2.4 it can be seen that the maximum penetration depth of the TFY signal is about $0.5\ \mu\text{m}$, the collected spectrum therefore corresponds to the volume within 500 nm of the surface.

$$P(x, E) = e^{-\alpha(E) \cdot x} \quad (2.2)$$

$$\alpha = \tau(E) \cdot \rho \quad (2.3)$$

Equation 2.2-2.3: Here P is the probability that the photon has not been absorbed by the material, E the photon energy, τ is the total attenuation (cm^2/g) and ρ is the density of the material.

At a photon energy of 350 eV, Si_3N_4 has a total attenuation of $4.31 \cdot 10^4\ \text{cm}^2/\text{g}$ and the density is $3.44\ \text{g}/\text{cm}^3$. At the same photon energy H_2O has a total attenuation of $8.06 \cdot 10^4\ \text{cm}^2/\text{g}$ and a density of $1\ \text{g}/\text{cm}^3$ [44].

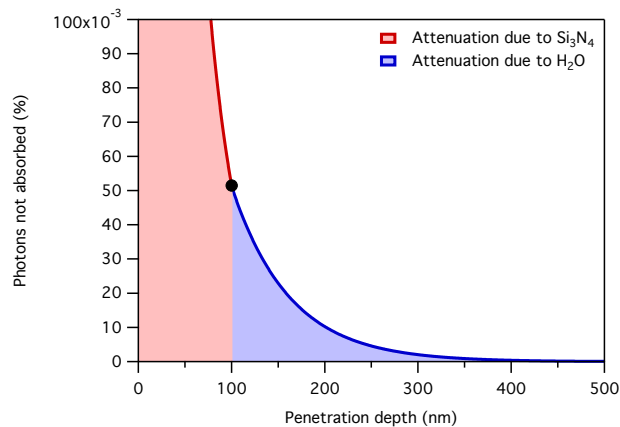


Figure 2.4: Here the attenuation length is calculated according to equation 2.2. The first 100 nm show a steep attenuation due to Si_3N_4 whereas beyond that the intensity is only attenuated by the presence of H_2O .

3. Results and Discussion

The first question that is posed is whether ex-vivo S-layers exhibit similar catalytic properties as their in-vivo counterparts with respect to the formation of CaCO_3 . Before focusing on the functional properties, a structural characterization of S-layers is made using high resolution in-situ AFM measurements.

3.1 Ex-vivo S-layer recrystallization

A culture of *Lysinibacillus sphaericus* is grown from which SbpA proteins are purified as is described in appendix C.1 [45, 16]. A freshly cleaved mica surface is exposed to 50 $\mu\text{g/ml}$ SbpA in a buffer solution (appendix C.2). The sample is left overnight and subsequently washed with deionized water to remove any excess SbpA monomers and free floating S-layers. The surface is then imaged using in-situ TappingMode AFM in deionized water.

In figure 3.1 one can observe the formation of S-layers with the typical square symmetry and lattice unit spacing of 13.1 nm as associated with S-layers from *Lysinibacillus sphaericus* [46, 47, 48].

As mentioned in section 1.1, the limiting step in the formation of S-layers is the formation of the tetrameric unit cell from four individual SbpA monomers.

The presence of defects can be seen in figure 3.1B. The two larger defects in the middle and to the right of the image show the incorporation of two incomplete tetramers, possibly trimers.

Furthermore it is interesting to see that the monocrystalline domains have formed two distinct height levels. The presence of multilayers can be ruled out based on the characteristic height of the S-layer. The S-layer height is found to be ~ 8 nm in liquid whereas the height difference between the two height levels is ~ 3 nm. Shin et al. showed that the different height levels are in fact different conformational states of the same S-layer proteins. During formation the S-layer can get trapped in a metastable state, which over the course of several hours transforms to a ‘taller’ thermodynamically stable conformer [12]. A recrystallization period of ~ 10 to ~ 20 hours ensures that most of the unstable S-layer domains have relaxed to their thermodynamic ground state. After this initial S-layer crystallization period continuous measurements of up to 40 hours showed no indication of structural changes, indicating the formation of a stable and immobilized S-layer.

From figure 3.1 it can therefore be concluded that SbpA monomers recrystallize on mica substrates ex-vivo while maintaining the same structure as observed in-vivo.

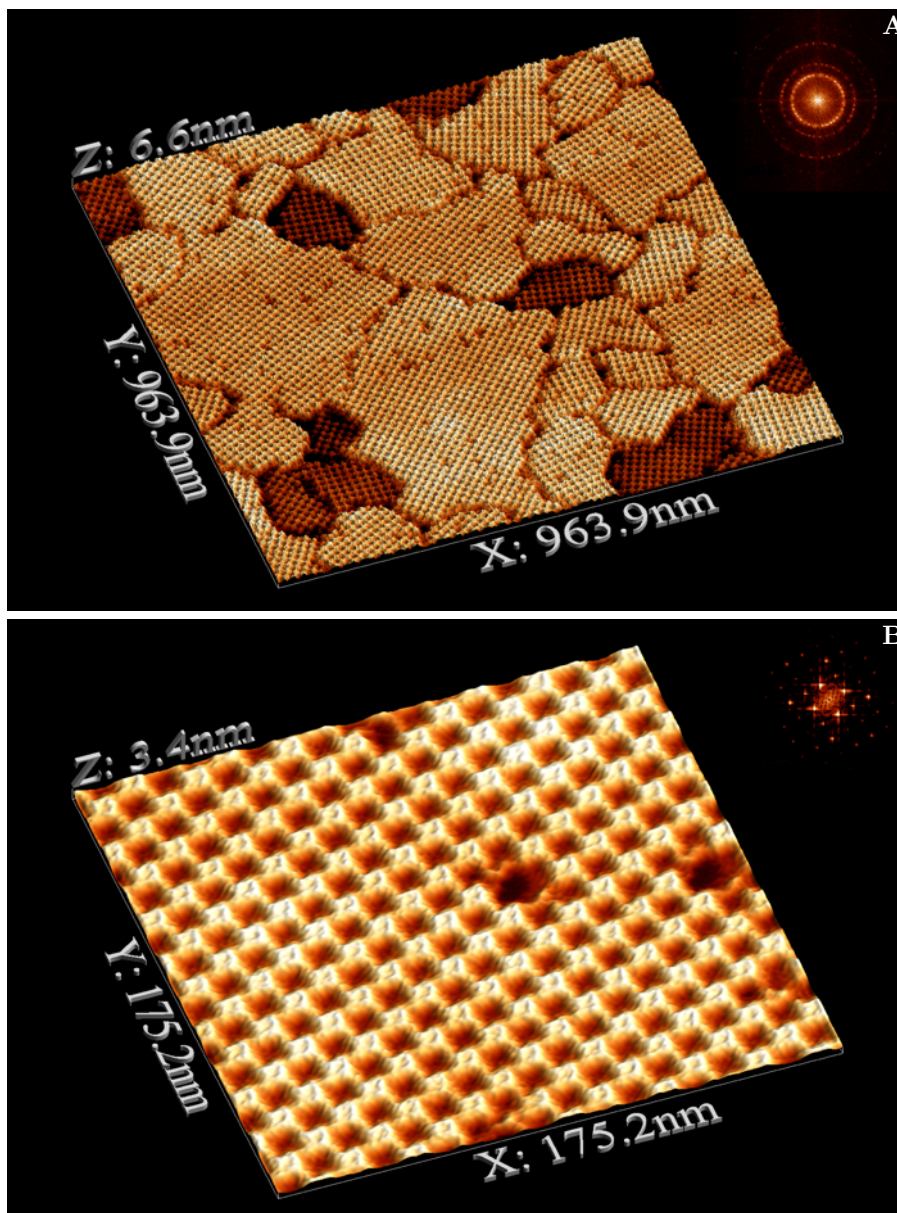


Figure 3.1: A high resolution AFM image of self-assembled S-layers crystallized ex-vivo by SbpA purified from from *Lysinibacillus sphaericus*.

(A) Multiple mono-crystalline S-layer domains. The random orientation of the various monocrystalline domains is nicely reflected by the circular pattern in the FFT spectrum.

(B) A single mono-crystalline domain. The characteristic square lattice can easily be observed and from the FFT spectrum the lattice constant is determined to be 13.1 nm. The smallest observable features are in the order of several nm.

The S-layer is crystallized following the protocol from appendix C.2. Imaged by in-situ AFM in TappingMode , Bruker FastScan-DX – 110 kHz, 0.25 N/m.

3.2 Calcium carbonate precipitation on immobilized S-layers

In order to probe the catalytic properties of S-layers in ex-vivo conditions they are recrystallized on a substrate and exposed to different concentrations of CaCl_2 and NaHCO_3 .

As described in equations 1.1-1.5 Ca^{2+} reacts with CO_3^{2-} to form solid CaCO_3 . Depending on the thermodynamic and kinetic properties of the system the CaCO_3 mainly forms a crystalline calcite structure or precipitates in an amorphous form appropriately called Amorphous Calcium Carbonate or simply ACC.

Three samples are prepared by recrystallizing S-layers on mica substrates as is described in appendix C.2. Subsequently the samples are exposed to concentrations of CaCl_2 and NaHCO_3 corresponding to natural lake conditions (10 mM and 3.2 mM respectively), below (equimolar at 3.5 mM) and above the homogeneous nucleation point of calcite (equimolar at 50 mM). In order to have a blank reference, three bare mica substrates are exposed to the same concentrations. All six samples are left to dry in a controlled environment to slow down the natural drying process.

The samples are imaged using optical microscopy and a clear difference can be observed between samples covered with S-layer and samples of bare mica that are used as a blank, figure 3.2.

At an equimolar concentration of 50 mM of CaCl_2 and NaHCO_3 there is clear

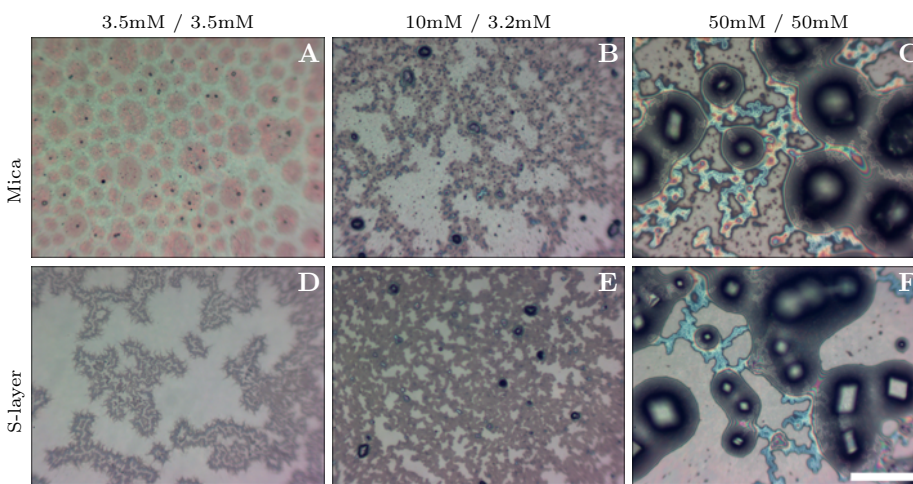


Figure 3.2: Images obtained with visible light microscopy. A comparison of bare mica samples versus mica + S-layers under exposed to CaCl_2 and NaHCO_3 at concentrations of 3.5mM/3.5mM, 10mM/3.2mM and 50mM/50mM respectively. All samples are covered with one drop of solution after which they are left to dry over the course of approximately two days before measuring. All images representative of the whole surface and are displayed at the same scale, the scalebar in (F) indicates 50 μm . S-layers on mica are grown by following the protocol in appendix C.2

evidence of the formation of calcite crystals in solution, figures 3.2(C) and (F). The big structures show the characteristic rhombohedral shape of calcite crystals. The fact that during AFM measurement these crystals were freely movable over the surface is consistent with the presence of calcite crystals nucleated in solution.

In figure 3.2(B) and (E) samples of mica and mica covered in S-layers are exposed to 10 mM of CaCl_2 and 3.2 mM NaHCO_3 . CaCl_2 and NaHCO_3 react in a 1:1 ratio to form CaCO_3 and during complete evaporation the excess Ca^{2+} , Na^+ and Cl^- will form CaCl_2 and NaCl .

The solubility in water of CaCl_2 is $9.6 \cdot 10^4$ times as high as the solubility of CaCO_3 (calcite) [49]. From this it is expected that calcite crystals will nucleate in solution before CaCl_2 will precipitate.

However instead of calcite crystals one can observe amorphous structures covering the surface with larger irregular shaped particles on top. Similar amorphous structures are observed at equimolar concentrations in (D) which suggests that CaCO_3 indeed precipitates before CaCl_2 , however not as calcite but as Amorphous Calcium Carbonate (ACC). The larger particles in figure 3.2(B) and (E) under these conditions are consistent with the presence of CaCl_2 and NaCl .

A classical nucleation picture states that the solubility of ACC is higher than the solubility of calcite [18, 49]. The presence of calcite in (C) and (F) is in agreement with this theory. However, the presence of S-layer in (D) and (E) show the enhanced formation of ACC and its stabilization at the interface.

The different solubility for ACC compared to calcite in combination with a dependence on time and surface chemistry makes the nucleation of CaCO_3 a complex phenomena.

However from the presence of ACC in 3.2(D) and the absence of ACC in 3.2(A) in combination with the higher density of ACC structures in 3.2(E) compared to 3.2(B) one can conclude that S-layers enhance the formation of Amorphous Calcium Carbonate (ACC).

3.3 ACC formation on S-layers investigated by AFM

To collect structural data of ACC formation on S-layers, this process is imaged using Atomic Force Microscopy (AFM). This can provide structural information about both S-layer and ACC formations on the nanometer scale.

In order to allow future in-situ X-ray absorption measurements that are directly comparable to AFM measurements, the substrate that is used has to enable S-layer immobilization as well as be transparent for X-ray photons. A substrate that has both of these qualities is Si_3N_4 [47].

The formation of ACC on S-layers is tracked in time by recrystallizing S-layers on Si_3N_4 substrates and subsequent exposure to CaCl_2 at 5 mM and an atmosphere of CO_2 created by the decomposition of NH_4HCO_3 in a closed desiccator. The CO_2 concentration in the enclosed environment will reach an equilibrium

with the carbonate content of the solution and when sufficient NH_4HCO_3 is present this equilibrium concentration can be maintained even when carbonate is removed from the solution by CaCO_3 precipitation.

Samples are removed after 30 minutes, 3 hours, 1 day and 3 days and subsequently washed and dried before imaged by AFM, see figure 3.3.

The S-layer structure is clearly visible in figure (F) and (G). On top of the S-layers the formation and growth of amorphous structures is observed. In (E) the round shape has a diameter of about 20 nm, 1.5 hour later these structures have grown to 30-60 nm and after 1 day the growth has spread out over hundreds of nanometers. Structural data obtained from these AFM images suggest these structures are composed of amorphous CaCO_3 . X-ray absorption spectra shown in figure 3.6 clearly identify the presence of ACC on these samples and will be discussed later in this chapter.

The concentration of 5 mM CaCl_2 lies below the nucleation point of calcite as well as ACC [18]. The formation of ACC at these concentration is therefore a further indication that S-layers are able to catalyze the formation of ACC.

While the diffusion of CO_2 into the solution is an effective method to maintain a constant concentration over time, it is not possible to easily control the actual concentration. Also liquid flow measurements are not possible because the use of a flow cell removes any liquid-air interface through which diffusion can take place.

Therefore in order to allow for future in-situ flow measurements that are directly comparable with ex-situ measurements it is preferred to use the mixing of known concentrations of CaCl_2 and NaHCO_3 .

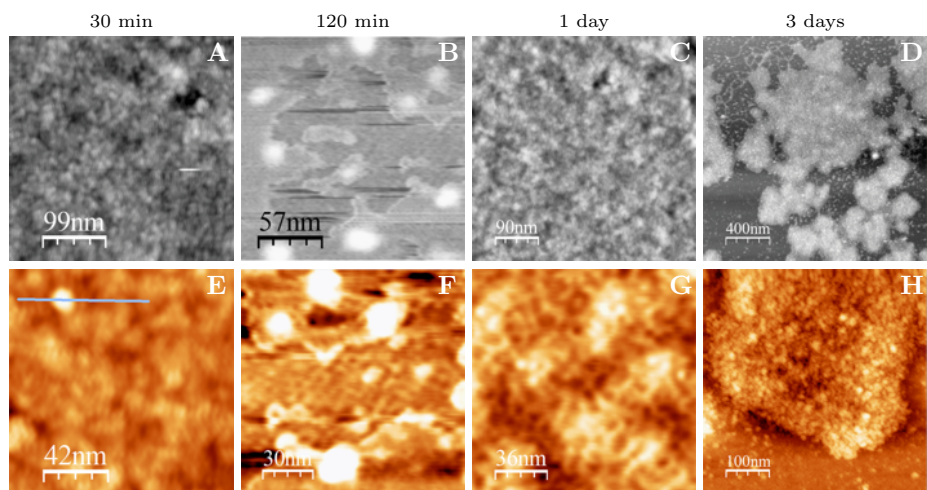


Figure 3.3: Images obtained by ex-situ AFM in TappingMode. The samples are prepared by recrystallizing S-layers on Si_3N_4 substrates and subsequent exposure to 5 mM CaCl_2 and an atmosphere of CO_2 which is maintained by the decomposition of $\text{NH}_4\text{HCO}_3(\text{s})$.

Samples are extracted after 30 minutes, 3 hours, 1 day and 3 days.

In figure 3.4 AFM images of samples exposed to different concentrations of CaCl_2 and NaHCO_3 are presented.

Samples are prepared by crystallizing S-layers on Si_3N_4 and a subsequent exposure to concentrations of CaCl_2 and NaHCO_3 triggers the formation of CaCO_3 on top of the S-layers. The formation of CaCO_3 is stopped after an incubation period of 1 hour by washing the surface with deionized water.

The concentrations of CaCl_2 and NaHCO_3 are 10 mM and 3.2 mM respectively – natural lake conditions – and an equimolar concentration at 3.5 mM, comparable to the concentration used in figure 3.3. As reference a blank Si_3N_4 surface is exposed to the equimolar concentration of 3.5 mM CaCl_2 and NaHCO_3 .

The AFM images from figure 3.4 show that the formation of CaCO_3 primarily happens on the S-layers and not on bare Si_3N_4 .

From the histograms in (D), (E) and (F) the height of the S-layers in air is ~ 4 nm. This is significantly lower than their height in liquid (figure 3.1). This difference is mainly due to a higher imaging force in air compared to liquid – a

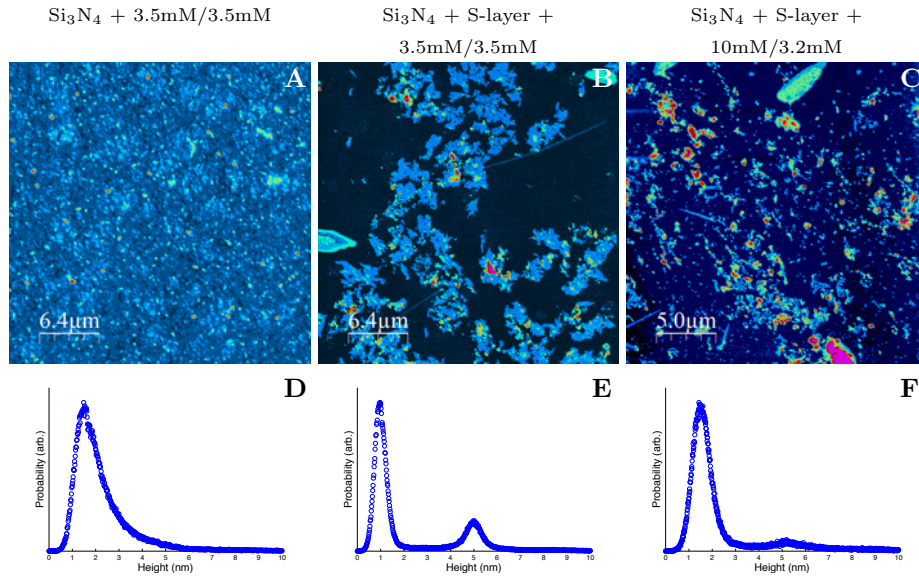


Figure 3.4: AFM measurements of CaCO_3 growth with and without S-layers present. All samples are exposed to CaCl_2 and NaHCO_3 at various concentrations for 1 hour before washing with deionized water. The height histogram data of the respective image is shown below. All S-layers are prepared according to appendix C.2.

(A) Si_3N_4 without S-layer. The absence of S-layer is also indicated by the single peak in the height histogram. The sample is exposed to CaCl_2 and NaHCO_3 at 3.5 mM.

(B) Si_3N_4 covered by S-layer. The S-layers are of uniform height, which is reflected in the height histogram (E) where a second peak is present ~ 4 nm higher than ‘ground’ level, indicated by the first main peak. The sample is exposed to CaCl_2 and NaHCO_3 at 3.5 mM.

(C) Si_3N_4 covered by S-layer (appendix C.2). From its histogram the S-layers height is again found to be ~ 4 nm higher than ‘ground’ level. However the height of the S-layer is masked by the addition of CaCO_3 structures on top, broadening the second peak in. The sample is exposed to CaCl_2 and NaHCO_3 at 10 and 3.2 mM respectively. Imaged by ex-situ AFM in TappingMode, Bruker FastScan-A – 1.4 MHz, 18 N/m.

cantilever with a spring constant of ~ 18 N/m in air versus 0.25 N/m in liquid. The S-layers are presented as the light blue patches ~ 4 nm above the ground level in (B) and (C) with the taller CaCO_3 structures shown in green ~ 10 nm, orange ~ 15 nm, red ~ 50 nm to magenta and blue again > 100 nm. CaCO_3 also appears to form on bare Si_3N_4 , however less dense and no larger structures are observed as can be seen in (A).

While the coverage of S-layer differs between samples, the percentage of S-layer that is covered in CaCO_3 is related to the concentration of CaCl_2 and NaHCO_3 , see also table 3.1.

From table 3.1 it can be seen that CaCO_3 predominantly precipitates on the S-layer patches. Almost no CaCO_3 structures are observed on bare Si_3N_4 when S-layers are present, figure 3.4(B) and (C).

In order to unambiguously identify the formation of ACC on S-layers we performed the spectroscopic measurements described in the next section.

	S-layer coverage (%)	CaCO ₃ coverage (10 ⁶ nm ³ /μm ²)	
		Overall	On S-layer
Si ₃ N ₄ + 3.5/3.5	–	0.3	–
S-layer + 3.5/3.5	32	0.47	1.5
S-layer + 10/3.2	20	1.8	4.5

Table 3.1: The CaCO_3 coverage of the AFM measurements in figures 3.4(A-C) is calculated using the histogram data from (D-F).

First the S-layer coverage is determined by calculating the coverage of all structures taller than about half the S-layer height indicated by the respective histogram. The S-layer height is measured in air and found to be ~ 4 nm. With this the total volume of S-layers can be calculated. The total total volume of CaCO_3 + S-layers can be calculated by determining the total volume of all structures taller ‘ground’ level, indicated by the main peak in the histograms. From this the total S-layer volume is subtracted and subsequent division by the total surface area gives the overall CaCO_3 coverage.

Since all CaCO_3 structures seem to be located on top of S-layers, the CaCO_3 coverage on S-layers is calculated by determining the total volume of structures taller than the S-layer height as indicated by the histogram, and subsequent division by the area covered by S-layers.

3.4 ACC formation on S-layers investigated by XAS

X-ray absorption spectroscopy measurements are done at the Advanced Light Source (ALS) located at the Lawrence Berkeley National Laboratory (LBNL). The ALS is a third generation synchrotron capable of accelerating electrons up to 1.9 GeV, producing a beam current of 500 mA.

During the course of this thesis a total of five beam times have been performed at beamline 7.0.0.1 and beamline 8.0.1.3. Both beamlines are capable of recording both the Total Fluorescent Yield (TFY) and the Total Electron Yield (TEY) at X-ray photon energies ranging from 80 to 1250 eV [50].

Calcium has several core electron shells that can be excited by incoming X-ray photons, depending on their energy. We used the energy range to probe the calcium L_{II} and L_{III} edge in CaCO₃ at 352.6 eV and 349.3 eV respectively [51, 52, 23, 53].

At these energies absorption of an X-ray photon will result in the excitation of a $2p$ electron from the L-shell. The reason for two distinct absorption energies is that through spin-orbit coupling the $2p^5$ electronic configuration is split into two separate energy levels, $2p^{1/2}$ and $2p^{3/2}$. The $2p^{1/2}$ state has slightly higher energy and excitation of a $2p^{1/2}$ electron to continuum will give rise to the L_{II} edge. The excitation of a $2p^{3/2}$ electron will then result in the L_{III} edge [54].

The NEXAS absorption spectrum of the Ca-L_{II} and L_{III} edge is given for three reference samples in figure 3.5. Following the analysis of de Groot et al. the peaks are labeled a_1 , a_2 , b_1 and b_2 . The two main peaks a_2 and b_2 represent the L_{III} and L_{II} edge respectively [55].

The origin of the secondary peaks a_1 and b_1 is known to be related to the crystal field splitting which arises from the non-spherical distribution of neighboring atoms around the absorbing atom. The negative charge of neighboring ions affects the d-orbitals in the absorbing atom. When the charge is distributed spherically all five d-orbitals are equally affected. However when ions are fixed in place due to a crystalline structure of the sample, the charge is no longer spherically distributed and each d orbital is affected differently. The result is a splitting of the energy levels of these orbitals [55, 56, 57].

The final $5d^{3/2}$ and $5d^{5/2}$ states of the L_{II} and L_{III} edge are affected by such a crystal field splitting and this creates extra energy levels available for the excited $2p^5$ electrons. This shows up in the spectrum as secondary peaks that precede the two main L_{III} and L_{II}, a_1 and b_1 respectively.

The position and intensity of the crystal field peaks is therefore a measure for the distribution of ions around the absorbing atom. In case of a strong crystal structure it is expected that the crystal field splitting will result in the presence of strong secondary peaks. In the case of an amorphous material without crystal structure the ions are expected to be distributed spherically around the absorbing atom which will therefore not result in a crystal field splitting and therefore the lack of crystal field peaks in the absorption spectra can be interpreted as the absence of a crystal structure of in the sample.

The relative small energy difference due to the spin orbit coupling for calcium in

combination with the small crystal field splitting produces a very characteristic $L_{III,II}$ XANES [58, 59, 51]. This makes XAS measurements at these energies a very effective tool to identify the morphology of calcium containing compounds.

All XAS measurements presented in this thesis probe the Ca $L_{III,II}$ -edge of the samples under investigation. Differences in the peak positions and intensities are then used to identify unknown compounds.

Recording of Ca $L_{III,II}$ -edge to distinguish between the different polymorphs of $CaCO_3$

The absorption spectrum can be measured by either collecting the TEY or TFY signal as is described in section 2.2.1.

The TEY detector available at beamline 8.0.0.1 has a better signal to noise ratio than the TFY detector, the opposite is true for beamline 7.0.0.1. Both spectra have a similar shape in most of the cases.

The goal of these measurements is to determine whether $CaCO_3$ is present in crystalline or amorphous form. In order to do this the spectra obtained from the samples are compared with spectra obtained from known references.

The references used during the ex-situ AFM measurements are shown in figure 3.5. All spectra are measured under UHV conditions and every point is an integration both in space and time. The spot size on the sample is approximately $100 \mu m \times 35 \mu m$ ($3.5 \cdot 10^3 \mu m^2$) and every point in the graph is the average intensity during an exposure of several seconds [50].

The S-layer reference is prepared by recrystallizing SbpA proteins on Si_3N_4 according to the protocol in C.2. The spectrum shown here is obtained by measuring the Total Electron Yield (TEY) as function of photon energy.

The calcite reference is prepared by cleaving a fresh natural calcite crystal – *Icelandic spar* (*Wards Natural Science, Rochester, NY*). The Total Fluorescence Yield (TFY) is collected in this case due to the poor conductivity of calcite, which results in a very weak TEY signal

The ACC reference is provided by Dr. Alejandro Fernandez-Martinez (LBNL) and consists of a synthetic ACC powder. Since ACC powder has a poor conductivity the TFY signal is measured as function of photon energy.

All samples are attached to a stainless steel sample holder with double sided copper tape, except reference containing ACC powder which has been fixed a similar stainless steel sample holder by using double sided carbon tape.

The crystal field peaks a_1 and b_1 are very pronounced for the calcite reference spectrum. The intensity of these peaks is a measure of the local order around the absorbing atom. Since calcite is of crystalline nature, we observe strong and sharp crystal field peaks (a_1 and b_1).

Apart from a shoulder at the b_1 position the ACC reference sample shows no well defined crystal field peaks. The absence of a crystal field suggest a spherical distribution of neighboring atoms around the absorbing atom and therefore the absence of local order in the sample. The ACC reference sample is clearly amorphous [23, 24].

The spectrum of the S-layer shows weak indications of crystal field peaks at both a_1 and a_2 positions. This can be explained by the fact that calcium is incorporated in the S-layer at specific sites where the Ca^{2+} absorbing atom is

surrounded by different neighboring atoms in a non-spherical distribution.

In figure 3.6 spectra obtained from various samples are compared with the reference spectra discussed before. The samples are prepared similar to the AFM images shown in figure 3.3 and can therefore be easily compared.

S-layers are crystallized on Si_3N_4 substrates as is described in appendix C.2. After this the samples are exposed to either CaCl_2 at 25 mM and incubated for 10 hours in an atmosphere of CO_2 or CaCl_2 at 50 mM and incubated for only 60 minutes in an atmosphere of CO_2

After the incubation period the samples are washed with deionized water to stop the formation of CaCO_3 and to remove any CaCO_3 not attached to the surface such as calcite crystals. After the samples have been dried they are attached to a steel plate and loaded into the XAS measurement chamber under UHV conditions at beamline 7.0.0.1. The TFY detector at this beamline provides a better signal-to-noise ratio than the TEY detector. This is the reason why all spectra are recorded by collecting the Total Fluorescence Yield.

The S-layer sample exposed to a low concentration of CaCl_2 , here shown in blue, has no sharp crystal field peaks. Based on the absence of a crystal field one can conclude that there must be a spherical distribution of neighbors around the absorbing atom which is indicative of an amorphous material. Indeed the spectrum closely resembles the reference spectrum of synthetic ACC powder.

The orange spectrum obtained from a sample that has been in contact with 50 mM CaCl_2 displays two clearly identifiable crystal field peaks at positions a_1 and b_1 . The position of these two peaks closely resembles the crystal field peaks

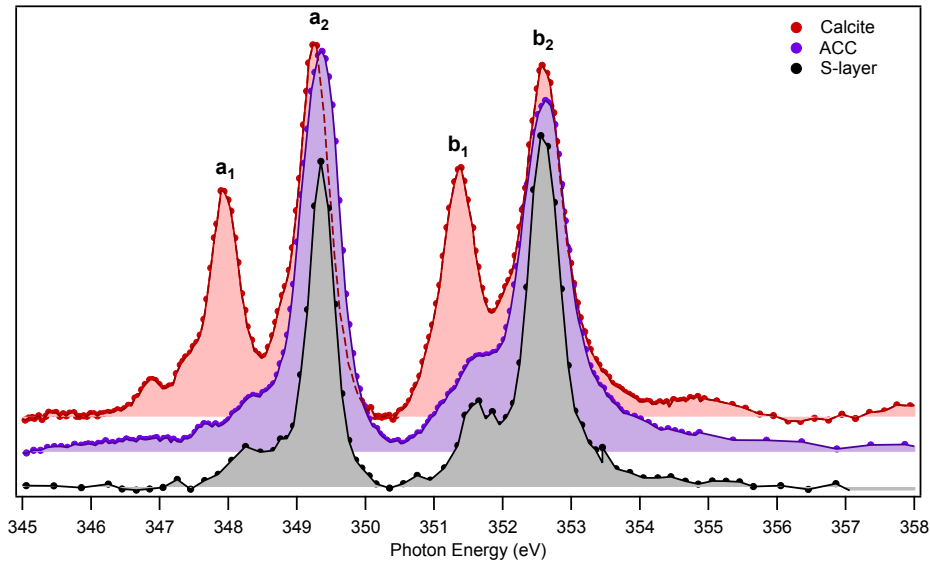


Figure 3.5: Reference spectra used during ex-situ XAS measurements. The S-layer reference is prepared by recrystallizing SbpA on a Si_3N_4 surface. The calcite sample is prepared by cleaving a natural calcite crystal and the ACC reference sample is provided by Dr. Alejandro Fernandez-Martinez (LBNL) and consists of a synthetic ACC powder. All spectra are analyzed as is described in appendix D.

of the calcite reference spectrum which indicates that also on this sample there must be crystalline calcite present. From figure 3.2 it is known that at equimolar concentrations of 50 mM CaCl_2 and NaHCO_3 calcite can homogeneously nucleate in solution. It is very likely that the same process occurs when 50 mM CaCl_2 is exposed to an atmosphere of CO_2 .

The spectrum that is displayed here in grey is obtained from an identically prepared sample as the spectrum displayed in orange. Here the crystal field peaks however are much less pronounced and the overall spectrum more closely resembles the S-layer reference than it does the calcite reference. The discrepancy between the orange and grey spectrum can be explained by considering that the washing procedure designed to remove all calcite crystals that nucleated in solution is not always 100% effective. Some calcite crystals can remain on the surface and when the X-ray spot on the surface coincides with the presences of a crystal, the absorption spectra will resemble that of calcite.

When the results from figure 3.6 and 3.3 are compared it is clear that ACC structures are stable on S-layers for more than 10 hours as observed by XAS and even up to 3 days as observed by AFM.

In order to have more control over the concentrations of both Ca^{2+} and CO_3^{2-} during CaCO_3 formation and to maintain comparability with the AFM mea-

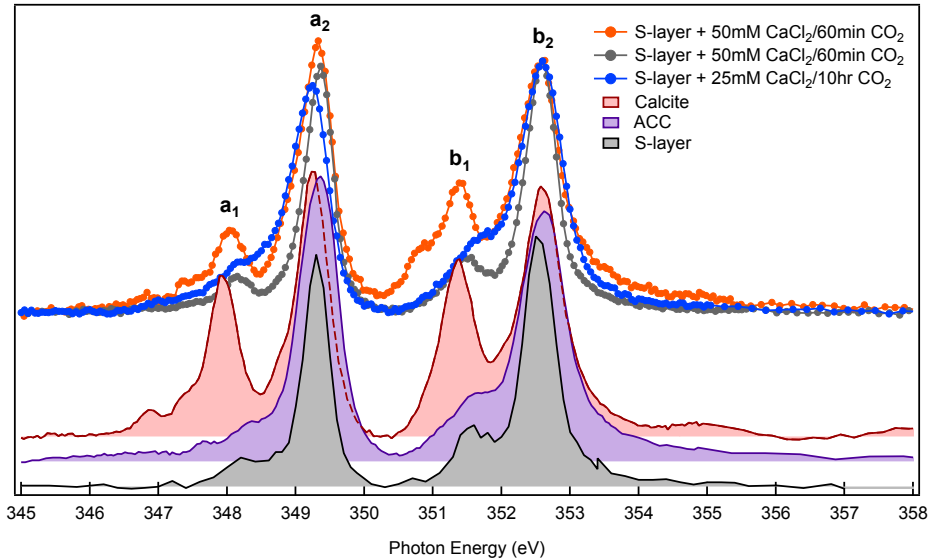


Figure 3.6: Here the X-ray absorption spectra of calcium are shown for different samples and compared to references. The samples are prepared by recrystallizing S-layers on top of Si_3N_4 conform appendix C.2 after which they are exposed to a drop containing CaCl_2 at 25 mM and 50 mM respectively in an atmosphere of CO_2 . The CO_2 triggers the formation of CaCO_3 on the S-layer surface as is described in section 1.2.

The X-ray absorption spectra obtained from these samples are compared with reference spectra of calcite, ACC and pure S-layer. For clarity an offset is introduced between the various reference spectra and S-layer samples. All spectra are analyzed as is described in appendix D.

measurements, the following XAS experiments are performed on samples that are exposed to CaCl_2 and NaHCO_3 at concentrations as found in natural lakes (10 mM and 3.2 mM respectively), below (equimolar at 3.5 mM) and above (equimolar at 50 mM) the nucleation point of calcite (equimolar at 13 mM).

In figure 3.7 three spectra are compared with the reference spectra from figure 3.5.

The measurements presented here are done at beamline 8.0.0.1 and the spectra are recorded by collecting the TEY signal.

The S-layers are recrystallized on Si_3N_4 according to appendix C.2 after which three samples have been exposed to the concentration mentioned before.

After an incubation period of 1 hour the samples are washed with deionized water to stop the formation of CaCO_3 and to remove any CaCO_3 not attached to the surface such as calcite crystals. After the samples have been dried they are attached to a steel plate with double sided copper tape and loaded into the XAS measurement chamber.

In figure 3.15 apart from the reference spectrum of calcite, no other spectrum shows a crystal field peak at position a_1 . At position b_1 only a shoulder can be observed in all measured samples. The absence of clearly defined crystal field peaks rules out the presence of calcite on the S-layer samples. Moreover the presence of a shoulder at position b_1 points to the presence of ACC.

When the same spectra are compared but now not normalized, as is shown in figure 3.16, it is clear that indeed ACC must be present on the S-layer samples.

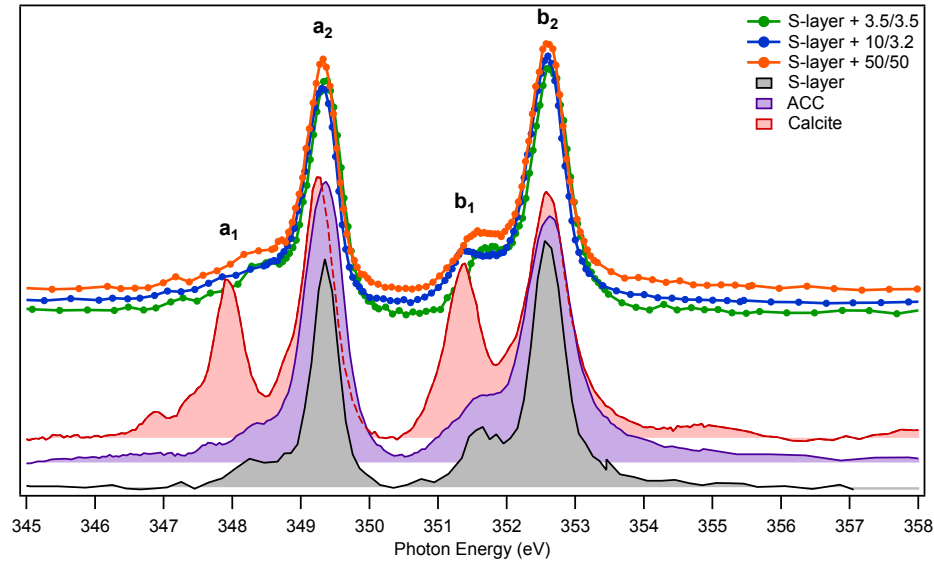


Figure 3.7: The largest three spectra from figure 3.8 are compared to spectra obtained from several reference materials.

The calcite reference spectrum is obtained from a freshly cleaved calcite crystal. The ACC reference is provided by Dr. Alejandro Fernandez-Martinez and consists of a synthetically produced powder of pure ACC. All spectra are normalized with respect to the second main peak at 352.6 eV and for clarity an offset is introduced between references and samples. Analysis is performed according to appendix D.

Bare Si_3N_4 and S-layer covered samples are exposed to the same concentrations of CaCl_2 and NaHCO_3 . The resulting absorption spectra on the bare samples show no difference with an empty Si_3N_4 reference sample that has been exposed to deionized water. The samples that had been covered in S-layer previous to exposure to CaCl_2 and NaHCO_3 however now measure TEY signals at intensities higher than can be explained by simply adding the TEY signals of the S-layer reference and the bare Si_3N_4 samples exposed to the same concentrations. Therefore the increase in intensity must originate in the formation of ACC.

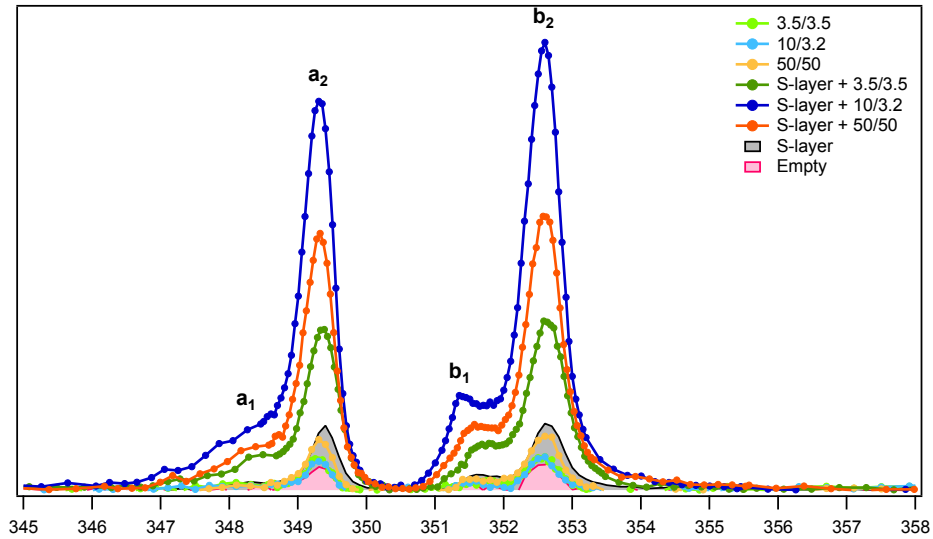


Figure 3.8: Here the X-ray absorption spectra of calcium are shown as measured on different samples. The spectra are not normalized, which means that the area below the curve is an indication of the total amount of calcium in the sample. The XAS data here is analysed using the method described in appendix D.

3.5 In-situ tracking of ACC formation on S-layers

Ex-situ optical microscopy, AFM and XAS measurements have shown that S-layers catalyze the formation of ACC.

However the question remains how the S-layer interacts with the CaCO_3 . The ex-situ measurements suggest the stabilization of ACC by the S-layer and in this section in-situ measurements are presented that try to capture the initial stage of CaCO_3 formation.

AFM liquid cell

The AFM liquid cell is designed to seal of a volume containing both the measurement area as well as the cantilever while at the same time allowing slight movement of the sample with respect to the cantilever in both lateral as vertical directions.

The liquid cell consists of a silicone cover that encompasses the measurement area and seals off an enclosed volume of liquid. The liquid cell includes an in- and outlet for liquid flows, allowing the exchange of solution during measurements.

3.5.1 In-situ AFM

The formation of structures on the surface of the S-layer is now tracked using in-situ AFM. The surface is first imaged in an inert environment of deionized water, after which this is replaced by the $\text{CaCl}_2/\text{NaHCO}_3$ solution and a continuous measurement is started. Continuous measurement times range from ~ 10 minutes up to more than a day.

The in-situ AFM measurements in figure 3.9 of mica covered in S-layers show that during a total exposure time of 7 hours no formation of solid calcium carbonate structures is observed.

The possibility that the measurement itself is inhibiting the growth is refuted by the fact that after the measurement area is moved; for example between (B) and (C) there is no observation of calcium carbonate in the newly scanned area.

From the AFM measurements in figure 3.4 it is expected that calcium carbonate structures will have formed on the surface as soon as 1 hour after exposure. A possible explanation for this discrepancy is that the formation of ACC structures happened outside the measurement area.

In figure 3.10 the in-situ measurements are now shown for a concentration of 10 mM CaCl_2 and 3.2 mM of NaHCO_3 over a 6 hour exposure. The concentration that is used here corresponds with levels that are naturally occurring in lakes [7]. The larger image (A) is made just before the solution was added to the sample and it already shows some particles attached to the surface. These particles can only be small contaminants left from the buffer solution used during the S-layer growth or small salt crystals or particles otherwise introduced to the system prior to the start of this measurement.

A detailed AFM image of two different pre-existing particles is shown in figure 3.11. Both particles have roughly the same shape, however the striking S-layer like pattern on top of the particle in (B) suggests that this one was present during the formation of the S-layer and that the S-layer simply has grown over

it [60]. It is therefore expected that particles like these do not change anymore during the measurements.

The particle in (A) however does not show an S-layer like corrugation, suggesting it is a contaminant that is introduced to the sample after the S-layer was formed.

From the four insets in 3.10(B) it is shown that these particles do not show any change during the 5.5 hours of exposure to the solution. An overview of the same area as 3.10(A) after 5.5 hours of exposure (not shown here) did not show any newly emerged particles.

While this is in agreement with what has been observed for the lower concentration of 3.5 mM, it is unclear what is the reason for lack of calcium carbonate growth.

The experiment shown in figure 3.12 gives further proof that no particles are growing or shrinking on the S-layer surface during even a 38 hour long exposure to a solution of 10 mM CaCl_2 and 3.2 mM of NaHCO_3 . A large area is imaged continuously for over 38 hours. The image shown in (A) shows an overview of

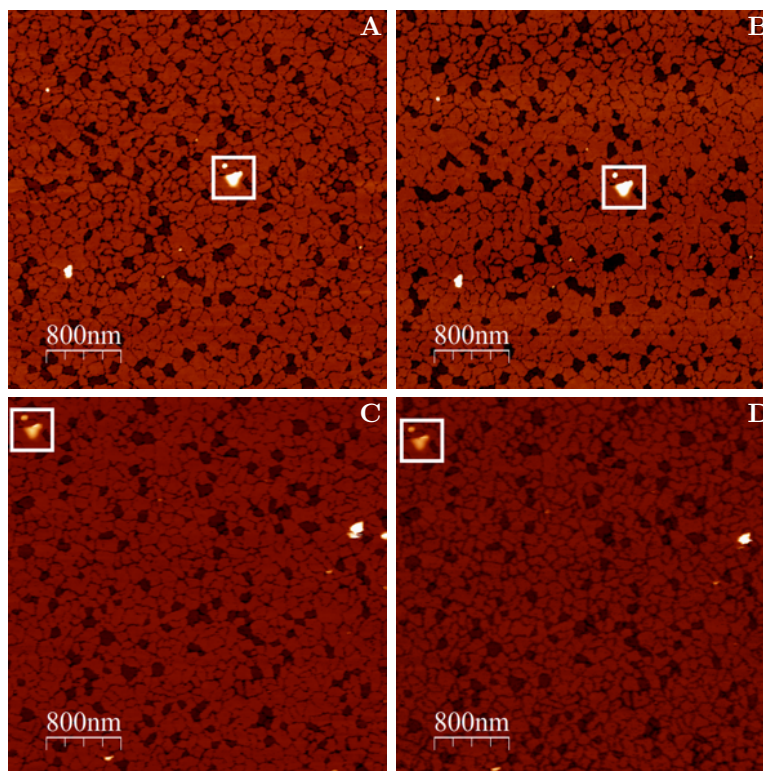


Figure 3.9: A mica surface covered with S-layer (appendix C.2) and exposed to CaCl_2 and NaHCO_3 at 3.5 mM.

Images (A-D) are snapshots taken 40 minutes, 3 hours, 4.5 hours and 7 hours respectively after continuous exposure of the surface to the solution. The measurement area has been shifted between (B) and (C), however their overlap is shown by the white square outlining a common feature in all images.

Imaged by in-situ AFM in TappingMode, Bruker FastScan-DX – 110 kHz, 0.25 N/m.

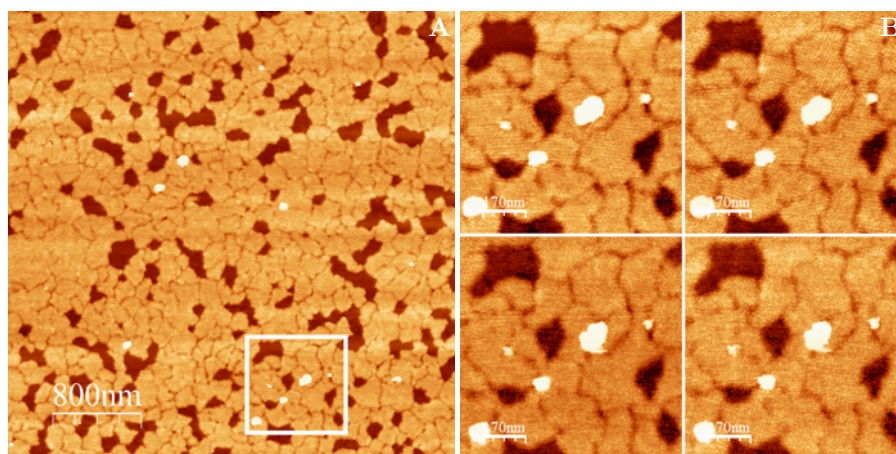


Figure 3.10: S-layer recrystallized on mica (appendix C.2) is exposed to CaCl_2 and NaHCO_3 at a concentration of 10 mM and 3.2 mM respectively, corresponding to naturally occurring lake levels [7].

(A) Shows an overview of the surface at the time of exposure to the solution. (B) Presents a zoom of the mid lower part of (A) after 1.5 hours (upper left), 3 hours (upper right), 4.5 hours (lower left) and 5.5 hours (lower right) after continuous exposure to the solution.

Imaged by in-situ AFM in TappingMode, Bruker FastScan-DX – 110 kHz, 0.25 N/m.

the measurement area, where (B) gives several height profiles which are plotted versus time. The corrugation in (B) is a result of drift correction. Apart from that there is no significant growth or dissolution of the particles as is indicated by their almost constant height profiles.

The triple nature of the features observed in (A) is most likely the result of contaminants on the AFM measurement probe, increasing its effective radius

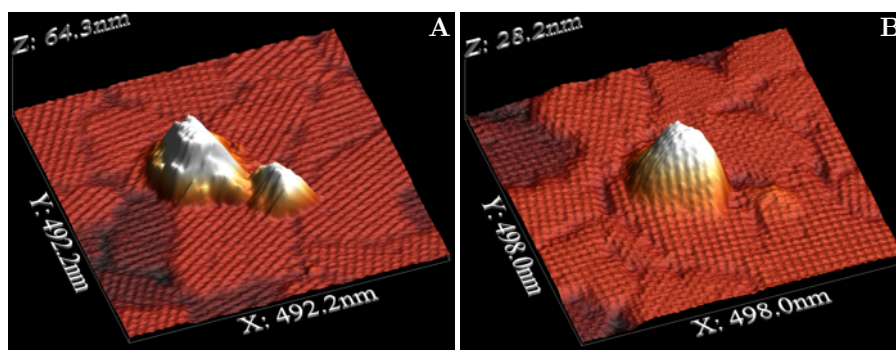


Figure 3.11: During the measurement presented in figure 3.10 two particles have been characterized in more detail.

(A) Shows a typical feature with smooth and jagged edges, hinting at height difference too steep for the AFM tip to track nicely.

(B) Shows a feature lower in height than (A). Also the corrugated surface seems to indicate that the S-layer has covered this feature.

considerably. When the sample features are much smaller than the probe which is used to measure them, they will reflect the shape of the tip rather than their own geometry [61].

In this measurement however, the main interest is the change in size of the sample features, which should still be observable, even with a measurement artifact like this. The varying line profiles in (B) can be explained by the fact that the tip contaminants have changed their shape slightly over the course of two days.

A mica substrate covered in S-layers and exposed to an equimolar concentration of 50 mM CaCl_2 and NaHCO_3 is presented in figure 3.13.

After multiple hours of exposure to the solution, no growth or otherwise change of surface features is observed, measurement results similar to figure 3.10 and 3.9 were obtained. However after a 30 minute incubation period during which the liquid flow cell was detached from the surface, the image shown in figure 3.13 here was acquired.

The fact that these structures only appeared on the surface of the sample after an incubation period away from the liquid cell reinforces the idea that during previous measurements the precipitation of CaCO_3 took place outside the measurement area. Possibly on the surface of the liquid cell which then lowered the effective concentration of the solution inside the cell.

A zoom is shown on the right side in figure 3.13(A), a second zoom is presented in 3.13(B). Here a sequential series of measurements shows that some features decrease in height by several nm, rightmost image in (B).

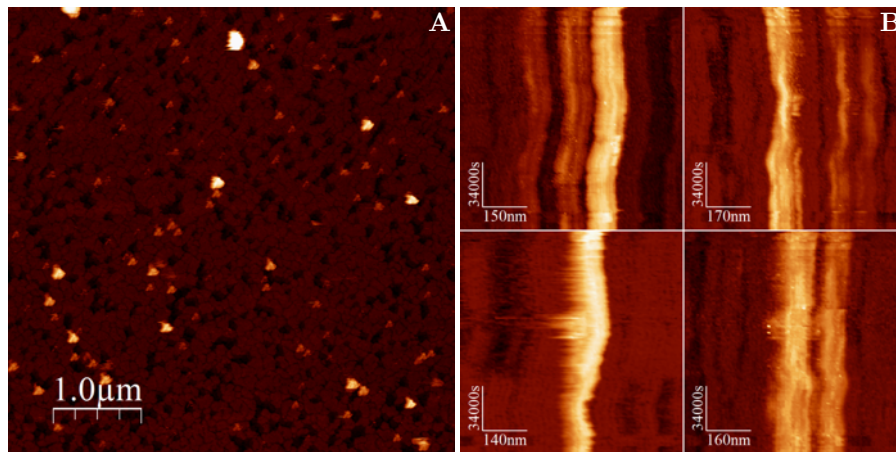


Figure 3.12: The experiment from figure 3.10 has been repeated here where the experiment has been allowed to run for more than 38 hours consecutively. Over this time more than 138 sequential images have been recorded. An overview is shown in (A). The four images in (B) show height profiles versus time for different features from (A). The perturbation that is seen is the result of drift. The triple nature of the features in (A) is due to contamination of the AFM probe and does not accurately reflect the feature shape. However information about size changes in time and number of particles can still be extracted.

Imaged by in-situ AFM in TappingMode, Bruker FastScan-DX – 110 kHz, 0.25 N/m.

Figure 3.14 shows AFM and optical microscopy images before and after leaving the sample in solution overnight.

The sample is imaged using the built in optical microscope of the FastScan AFM system. When 3.14(A) is compared with 3.14(B) it is seen that the amount of crystals on the surface has increased overnight while amorphous structures almost completely disappeared. This is in agreement with reports that show the depletion of ACC on SAMs in the presence of calcite crystals [19, 62]. This leads to the conclusion that after an initial fast growth, these amorphous structures slowly dissolve again.

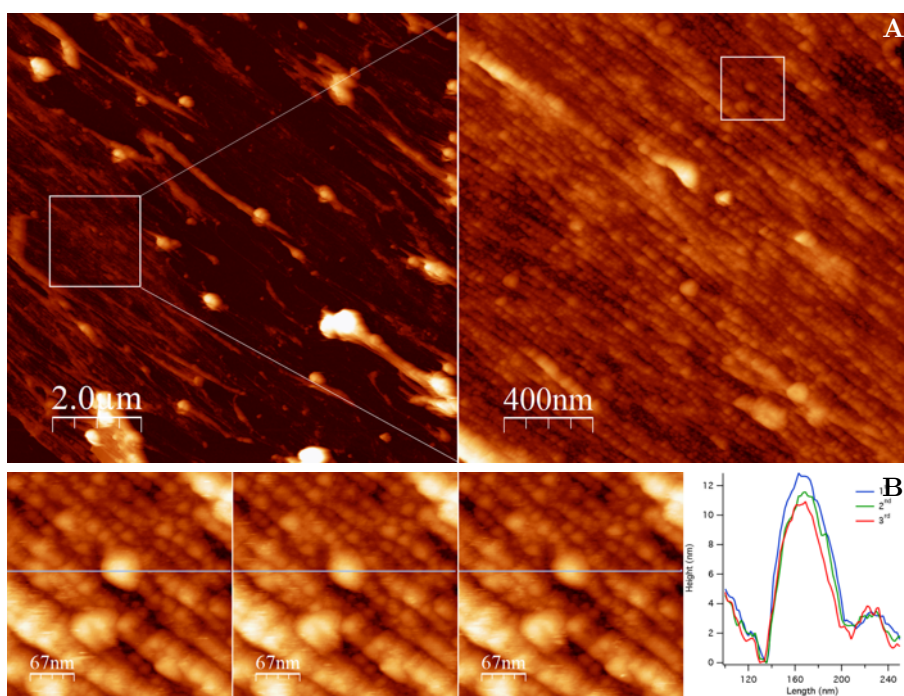


Figure 3.13: A similar sample as is used in figure 3.9 and 3.10 is here exposed to a solution containing CaCl_2 and NaHCO_3 at 50 mM. Well above the nucleation point of calcite. In (A) it is shown that large amorphous structures have emerged on the surface of the S-layer. The magnification on the right hand side shows a very high coverage in what seems to be linear amorphous structures. A sequential series of measurements on these structures is shown in (B). It is shown that parts of these structures shrink with the passing of time. The time between the first and last measurement is about 30 minutes.

Imaged by in-situ AFM in TappingMode, Bruker FastScan-DX – 110 kHz, 0.25 N/m.

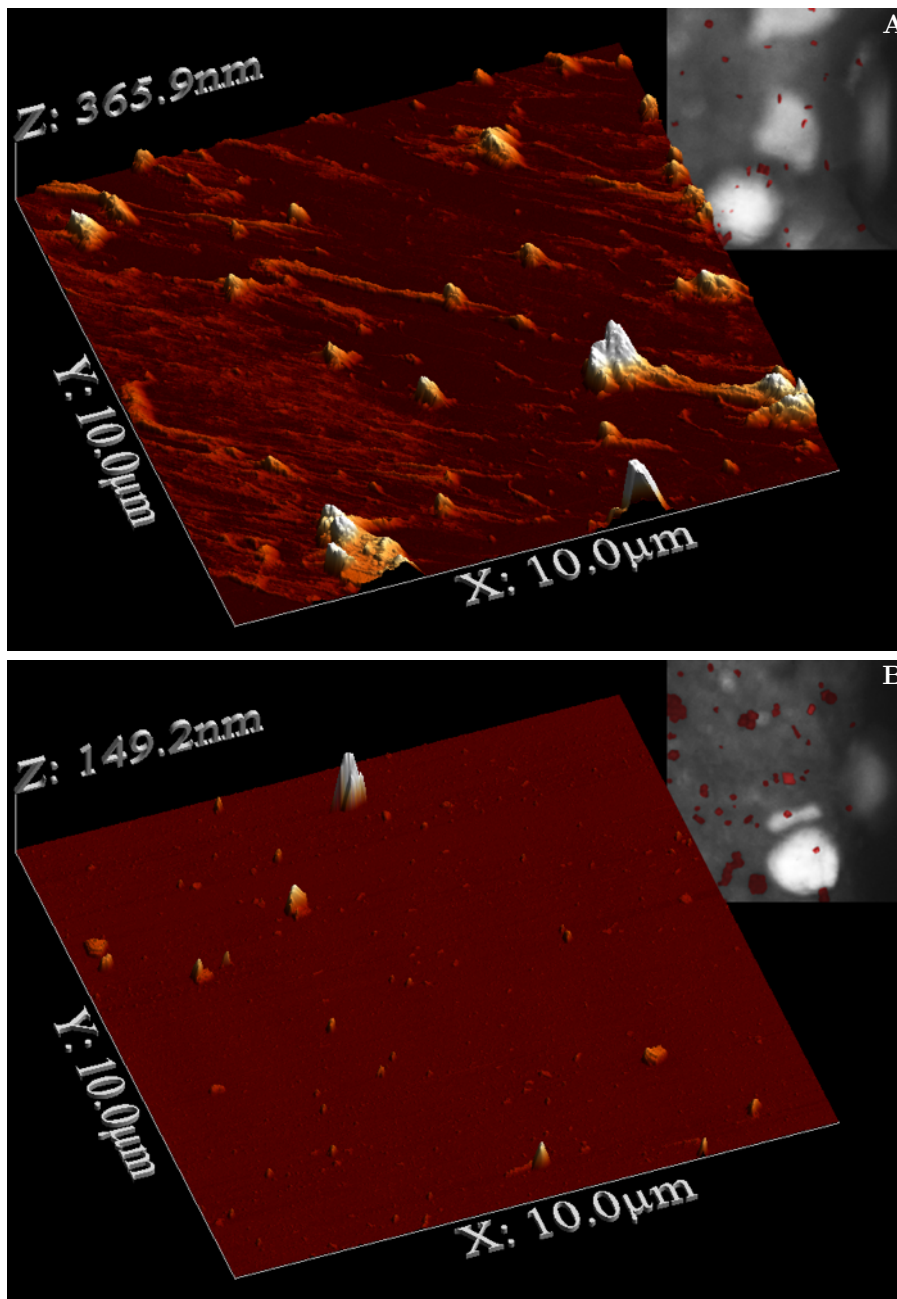


Figure 3.14: The observed amorphous structures from figure 3.13 are left overnight and imaged again. (A) The same image as in figure 3.13a. The inset in the right upper corner shows the amount of calcite crystals present on the sample during the acquisition of the AFM image. These optical microscopy images are made using the build in microscope of the FastScan system. For clarity the calcite crystals have been colored red. (B) After leaving the sample in the same solution overnight, the structures have dissolved. Again, the inset in the upper right corner shows the crystals present at the acquisition of (B).

Imaged by in-situ AFM in TappingMode, Bruker FastScan-DX – 110 kHz, 0.25 N/m.

3.5.2 In-situ XAS

In figure 3.15 a series of in-situ XAS measurements is compared to in-situ references of calcite, ACC and pure S-layer.

From previous measurements (figure 3.2(C) and (D)) it is known that calcite crystals will form in an equimolar solution of CaCl_2 and NaHCO_3 at 50 mM. This preparation is therefore used as in-situ calcite reference. The in-situ S-layer is prepared identical to the ex-situ S-layer reference but is now measured while contained in the liquid cell.

It is not possible to prepare the in-situ ACC reference by dissolving synthetically prepared ACC powder. This will simply result in a certain concentration of Ca^{2+} and CO_3^{2-} in solution.

The in-situ ACC reference is made by adding 1 ml CaCl_2 at 100 mM to 18 ml poly acrylic acid (PAA, Mw=5100 Da) at 250 ppm. After this 1 ml Na_2CO_3 at 200 mM is added. The function of the added PAA is to stabilize the ACC particles, which normally will redissolve to form thermodynamically more stable calcite crystals [19, 62].

S-layers are recrystallized on four different Si_3N_4 samples according to appendix C.2. After this the samples are placed inside the liquid cell as shown in figure 2.3.

Sealed together with the S-layer inside the cell is a solution containing CaCl_2 and NaHCO_3 at different concentrations. Concentrations are used that correspond to natural lake conditions (10 mM and 3.2 mM respectively), below (equimolar at 3.5 mM) and above the nucleation point of calcite (equimolar at 50 mM). The liquid cell is attached to a metal sample holder using double sided copper tape.

In figures 3.15 and 3.16 the XAFS obtained from the samples is compared the in-situ references.

In figure 3.15 it is interesting to see that although from previously described measurements it is clear that calcite is formed in solution at concentrations of 50 mM of CaCl_2 and NaHCO_3 , the absence of crystal field peaks at a_1 and b_1 in the in-situ calcite reference points to the opposite. The most straightforward explanation is that the calcite crystals are free-floating and are therefore not within the $\sim 500 \mu\text{m}$ that is accessible by collecting the TFY signal, see figure 2.4.

When the absence of calcite as described above is taken into account, the in-situ measurements correspond quite well to their ex-situ counterparts.

The blue and green spectra correspond to S-layers exposed to CaCl_2 and NaHCO_3 concentrations below the nucleation point of calcite. The presence of a crystal field peak at b_1 and the absence of a peak at a_1 combined with the overall shape of the spectrum which is very similar to the in-situ ACC reference, points to the presence of ACC on the S-layer surface.

When a concentration above the nucleation point of calcite is used – the orange spectrum in figure 3.15, the crystal field peak at position b_1 has decreased and is now more similar to the shape of the in-situ calcite reference. This is to be expected considering that the only difference between these two samples is the presence or absence of S-layers. The absence of ACC on the S-layer surface can

be explained by considering that the equilibrium concentration of CaCO_3 in solution in the presence of heterogeneous nucleation is lower than the solubility limit of ACC on S-layers, see also figure 3.2(F).

When the same data is presented but now not-normalized as is shown in figure 3.16, the presence of ACC on S-layer samples is even more clear.

Similar as in the ex-situ measurements presented in figure 3.8, the combination of S-layer and a concentration of CaCl_2 and NaHCO_3 below the nucleation point of calcite results in a large increase in X-ray absorption probability at the calcium edge compared with the pure S-layer reference. This indicates calcium precipitation near the S-layer surface.

Overview

In figure 3.17 AFM images are displayed along side their corresponding ex-situ and in-situ XAS measurements. All measurements shown here are already presented earlier in this thesis.

Figure 3.17(B) shows the XAFS in red of a Si_3N_4 substrate exposed to an equimolar concentration of 3.5 mM CaCl_2 and NaHCO_3 . The reference spectra are a freshly cleaved calcite in yellow, synthetic ACC powder in blue, an empty Si_3N_4 substrate in grey and pure S-layer in black, see figure 3.5. The intensity of the L_{II} edge in all reference spectra is normalized to 1, the intensity of the

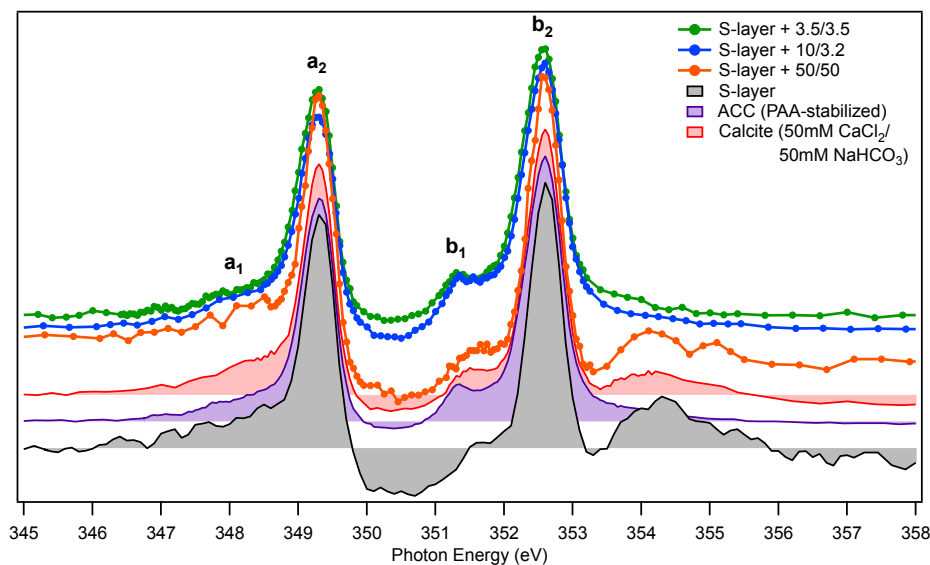


Figure 3.15: In-situ X-ray absorption spectra of calcium obtained by collecting the TFY signal. S-layers are recrystallized on Si_3N_4 following appendix C.2 and exposed to different concentrations of CaCl_2 and NaHCO_3 . The X-ray absorption spectra are compared to reference spectra of calcite, ACC and pure S-layer which are obtained by collecting the TFY signal as well.

The spectra displayed here have been analyzed using the method described in appendix D and for clarity an offset is introduced between samples and references.

XAFS in red and the empty Si_3N_4 reference in grey is scaled so as to preserve the relative intensities compared to the S-layer reference. This is done to show that the absorption spectrum of this sample is only marginally stronger than the empty reference, indicating that there is almost no calcium present on the surface. This is in agreement with what can be seen in (A), where there are only small structures present.

Figure 3.17(D) the XAFS of S-layer exposed to 10 mM CaCl_2 and 3.2 mM of NaHCO_3 is shown in red, where the dashed lines correspond to in-situ measurements and the solid lines to ex-situ measurements. The small crystal peaks at a_1 and b_1 resemble a mixture between the ex-situ ACC reference and the ex-situ S-layer reference. This corresponds with AFM image in (C) where only a small percentage of the S-layer surface is covered in CaCO_3 structures.

The in-situ XAFS however closely resembles the in-situ ACC reference. The overall shape as well as the presence of a single crystal field peak at position b_1 indicate that that a large percentage of the overall XAFS signal is due to ACC. The distribution of CaCO_3 structures is not uniform as can be seen in (C), this could be the reason for the discrepancy between ex-situ and in-situ spectra.

Figure 3.17(F) shows the in-situ and ex-situ XAFS of S-layer exposed to a concentration naturally found in lakes, i.e. 10 mM CaCl_2 and 3.2 mM NaHCO_3 . Both spectra are almost completely identical to the in-situ reference spectrum of ACC. When compared to the AFM image in (E) it can be seen that the surface is indeed covered in numerous ‘tall’ ACC structures.

From (A,C,E) it can be seen that when S-layers are present, structures form on S-layers and from (B,D,F) it is observed that these structures are composed of ACC.

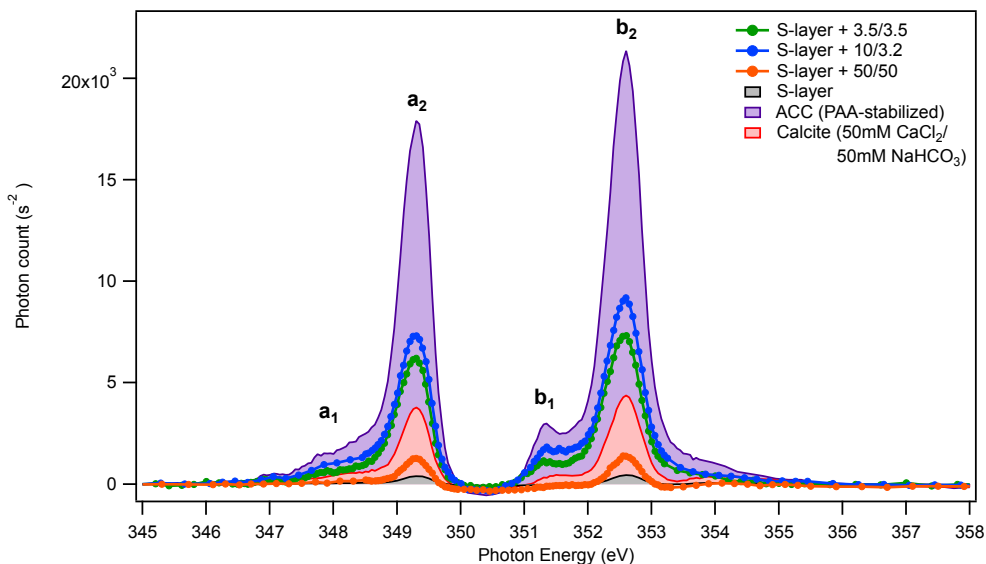


Figure 3.16: The same set of spectra as is shown in figure 3.15 is here presented without normalization. The area enclosed by the spectrum is a measure of the amount of calcium present in the sample.

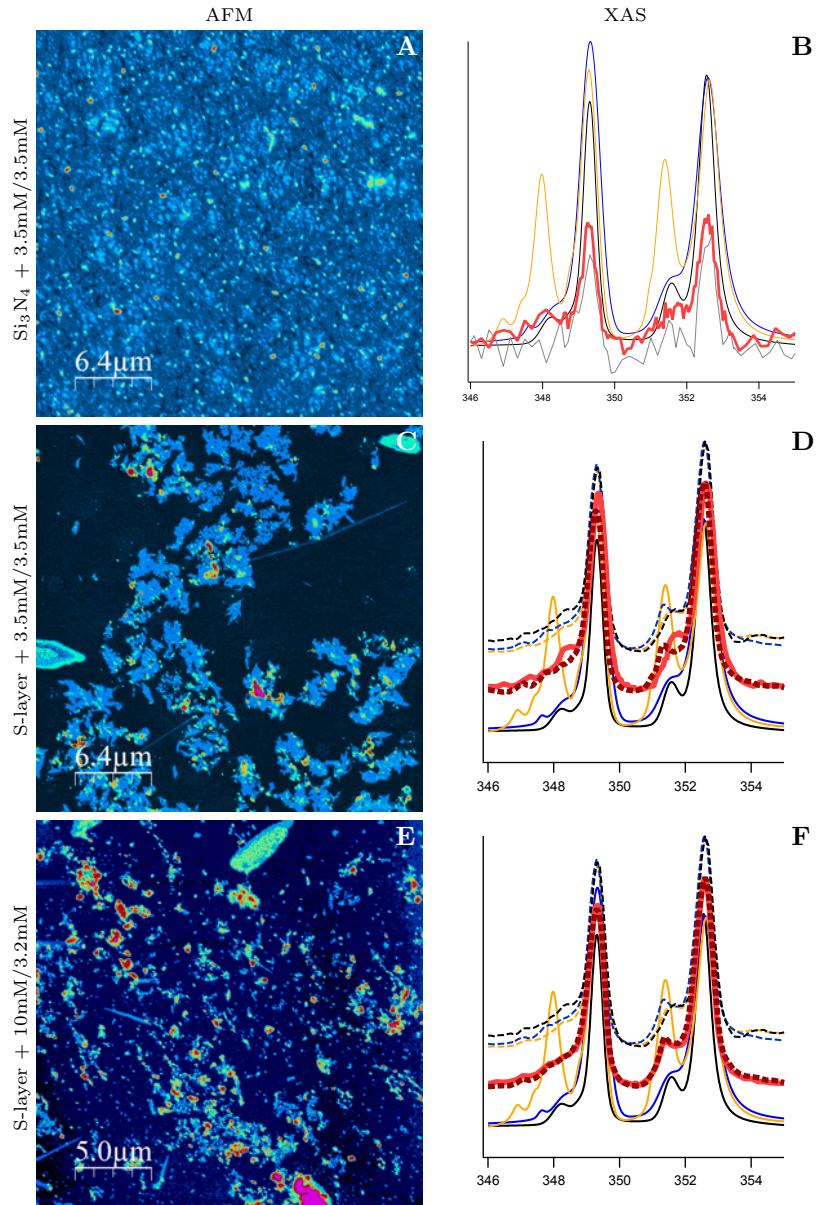


Figure 3.17: AFM measurements done on $\text{Si}_3\text{N}_4 + \text{S-layer}$ are compared with their respective in-situ and ex-situ XAS measurements. The XAS spectra in the last column are compared with reference spectra of calcite (yellow), ACC (blue), empty Si_3N_4 in grey and pure S-layer (black). The dashed lines represent in-situ measurements and the solid lines represent ex-situ measurements. The intensities of the spectra are normalized to 1 with exception of the red and grey curves in (B) which have been scaled so as to preserve their relative intensity compared to the S-layer reference.

4. Conclusion and outlook

4.1 Conclusion

By purifying and subsequently recrystallizing SbpA protein on both mica and Si_3N_4 substrates it is shown that S-layers can be recrystallized ex-vivo while maintaining their native structural properties.

It is shown that immobilized S-layers exhibit catalytic properties with regards to the formation of CaCO_3 . CaCO_3 precipitation on S-layers has been observed at concentrations far below the nucleation point of calcite or the solubility limit of ACC. Once formed these precipitates are found to be stable for several days. Furthermore by combining AFM with XAS the CaCO_3 precipitates are convincingly identified as Amorphous Calcium Carbonate.

It can therefore be concluded that S-layers both catalyze and stabilize the formation of ACC.

At super saturated conditions of CaCl_2 and NaHCO_3 in-situ AFM measurements have shown the rapid formation of ACC at the S-layer-liquid interface followed by a slow dissolution. Subsequent increase in calcite crystals in solution has been observed.

The mechanical details of how ACC transforms to calcite and whether this happens at the surface or in solution remain as open questions and we have designed a set of new experiments involving both AFM and XAS liquid flow measurements in order to get a deeper understanding of this process.

Furthermore, the combination of in-situ XAS and AFM in liquids proves to be a powerful experimental approach. It offers both high temporal and spacial resolution in combination with chemical as well as structural information and can be used to tackle many open questions on self-assembly and crystal growth. Recent advances in high speed AFMs and the development of better liquid cells for in-situ XAS will open up new experimental possibilities to extend our approach to biomolecular systems.

4.2 Outlook

The experimental nature in combination with the setting up of a new lab resulted in a very challenging research experience. During many experiments there were complications which triggered new ideas and possible improvements

on the measurement systems. This is a process that has not stopped and in this section I will explain several ideas on how to improve the experimental setup that has been used during this thesis.

In-situ AFM measurements

The formation of calcite crystals on the surface of the fluid cell poses a great challenge in using the flow cell system during these experiments. It is difficult to determine whether the CaCl_2 and NaHCO_3 concentrations that arrive at the sample surface are really the same as the concentrations that enter the cell.

A different approach to the flow cell system has been provided Dr. Jim DeYoreo. It has been suggested to use a system which will release carbonate slowly over time, directly at the surface of the sample. A system like this can be constructed by mixing a dialkylcarbonate with NaOH. Over time the dialkylcarbonate will get hydrolyzed by the NaOH which will release carbonate. Since this is a continuous reaction, the carbonate content will slowly rise with time. By selecting the NaOH concentration the final CO_3 concentration can be set.

Ideally this solution is continuously flowed over the sample by use of a syringe pump so as to avoid local depletion of the solution at the sample surface.

In-situ XAS measurements

Another improvement over the current static liquid cell experiments would be the implementation of a flow cell system. In this way the formation of calcium carbonate structures could be tracked with XAS in real time.

In combination with the improved flow cell set-up for the AFM this could provide a better understanding on how ACC will first form on and later dissolve again from the surface of the S-layer as function of the concentration.

We are currently setting up a liquid flow cell system for our experiments at beamline 8.0.0.1 at the Advanced Light Source.

z

5. List of presentations

During the course of this thesis I have presented parts of this work at several occasions. Here a chronological list:

29th Annual SAOG Meeting – Fribourg, Switzerland - January 25

Poster title: *Unraveling Mechanisms of CO₂ Sequestration on Self-Assembled Bacterial Surface Layers*

List of authors: Bart Stel, Seong-Ho Shin, Klaus Kern, Jim De Yoreo and Magalí Lingenfelder.

A one day symposium with changing topics in the field of surface and interface sciences. Participants had the opportunity to present their work in the form of a poster during the poster sessions.

CECAM workshop March 2013 – Lausanne, Switzerland - March 4-6

Self-assembly: from fundamental principles to design rules for experiment.

Poster title: *Directed Self-Assembly of Bacterial Surface Layer Proteins and Mechanisms of CO₂ Sequestration*

List of authors: Bart Stel, Ilja Gunkel, Seong-Ho Shin, Thomas Russel, Klaus Kern, Jim De Yoreo and Magalí Lingenfelder.

A 3-day workshop located at the EPF in Lausanne, Switzerland. Participants had the opportunity to present their work in the form of a poster during the poster sessions.

The Max-Planck-EPFL Winter School March 2013 – Tegernsee, Germany - March 10-15

Winter School on Chemical Reaction Dynamics at Surfaces.

Title of poster and talk: *Directed Self-Assembly of Bacterial Surface Layer Proteins and Mechanisms of CO₂ Sequestration*

List of authors: Bart Stel, Ilja Gunkel, Seong-Ho Shin, Thomas Russel, Klaus Kern, Jim De Yoreo and Magalí Lingenfelder.

A 5-day event located at Schloss Ringberg in Tegernsee, Germany. Participants had the opportunity to present their work in the form of a poster and a talk.

6. Acknowledgments

Foremost I would like to thank my supervisor Dr. Magalí Lingenfelder for offering me the great opportunity to perform this research at her group at the Max-Planck-EPFL Center. For her constant support, engagement and continuous effort to bring out the best in the people around her. She showed me the ins and outs of not only academical research itself but also introduced me to the fascinating world around it.

I also want to thank prof. Dr. Frieder Mugele and Dr. Ir. Harold Zandvliet for their support and flexibility with regards to all logistical and bureaucratic matters that come along with performing this Master research abroad.

I want to thank prof. Dr. Klaus Kern for offering me the possibility to work at the Max-Planck-EPFL Center.

Of course I want to thank the other members of the group, Dr. Gustavo Ruano and Dr. Fernando Cometto for all the interesting and useful discussions on a variety of topics including, but not limited to, this research.

At the EPFL I further want to thank Gilles Grandjean and his team for all the technical support on building up the labs and Angeles Alarcon for her assistance on all paperwork.

At the LBNL I want to thank Dr. Behzad Rad for his help at the Molecular Foundry on purifying the SbpA protein. I thank Dr. Ilja Gunkel for his collaboration on the project about directed self-assembly on block-copolymers and the great work he has done on the fabrication of linear line patterns. And I want to express my gratitude to Xuefei Feng from the group of Jinghua Guo for always being there to help during the beamtimes at the ALS.

I also want to thank Dr. Jim de Yoreo for his discussions and clear insights on almost any topic. His vast knowledge and experience on self-assembly and crystal growth proved invaluable.

And of course thanks to Dr. Jinhui Tao and Dr. Alejandro Fernandez-Martinez for providing the ACC reference samples.

A. Directed self-assembly of bacterial surface layer proteins

Apart from investigating carbon mineralization on S-layers during this thesis, we explored how to direct self-assembly and protein crystallization at the nanoscale. In this appendix it is shown that the directed self-assembly of SbpA is achieved by crystallizing it on block-copolymer thin films consisting of PolyStyrene (PS) and Polyethylene Oxide (PEO). This method allows us to effectively control protein crystallization at the nanoscale.

We plan to extend this approach to other relevant proteins like collagen.

By manipulating the molecular weight and the ratio between compounds in a diblock-copolymer system, it is possible to create well-defined patterns [63, 64, 65, 66].

Block copolymers (BCs) consist of two polymers with different chemical properties which are bonded together through covalent bonds. The chemical properties of the BC constituents can be chosen so that demixing will occur. However due to the covalent bonds binding the complex together, demixing is not possible and instead phase separation will occur. The scale of the resulting pattern is directly related to the length of the polymer chains, i.e. molecular weight [63]. The formation of block copolymer thin films is especially interesting due to the strong influence of surface topography of the underlying substrate and tunable ratio of BC constituents on the resulting pattern [65, 64].

It is shown that by templating the self-assembly of SbpA on PS-PEO block-copolymer thin films the S-layer formation is confined to the hydrophobic PEO regions that appear higher in figure A.1(A). The crystalline nature of the S-layer is preserved during confinement, and the orientation of the S-layer lattice is aligned with the underlying pattern, figure A.1(C).

The size of the monocrystalline domains in figure A.1(C) appears to be limited by the curvature of the underlying block-copolymer system.

In order to investigate this effect further a unidirectionally aligned BC pattern is designed by using the surface topography of a faceted sapphire substrate [66]. Unidirectional line patterns are interesting as substrates for epitaxial oriented growth of materials in numerous research fields [67, 68]. This includes liquid crystals [69], polymers [70], small organic molecules [67], organic dyes [71] and

enzymes like myosin [72].

The alignment of BC patterns on surfaces is driven by the entropy of chain packing and the final configuration therefore represents the free energy minimum of the system. The sapphire substrate has a unidirectional line pattern with a line spacing of ~ 130 - 165 nm and its interaction with the block-copolymer on top drives the formation of a unidirectional packing of the block-copolymer, see figure A.2.

Preliminary experiments with SbpA self-assembly on linear aligned line patterns has shown a critical dependence of the linewidth on the confinement of the S-layers. The line spacing of the lamellar line pattern in figure A.2(B) is ~ 50 nm and shows good confinement properties whereas the linear line pattern in figure A.3 has a ~ 30 nm line spacing and shows S-layers that encompasses multiple lines.

By designing linear aligned BC patterns with line spacings around ~ 50 nm we aim to direct the self assembly of S-layer into linear stretches while preserving their internal crystalline configuration.

In-situ self-assembly experiments will help us to shed light onto the growth mechanism of SbpA on BC patterns.

These preliminary results indicate block-copolymers might pave the way for controlling protein crystallization in well defined nanoscale patterns that extend over cm areas.

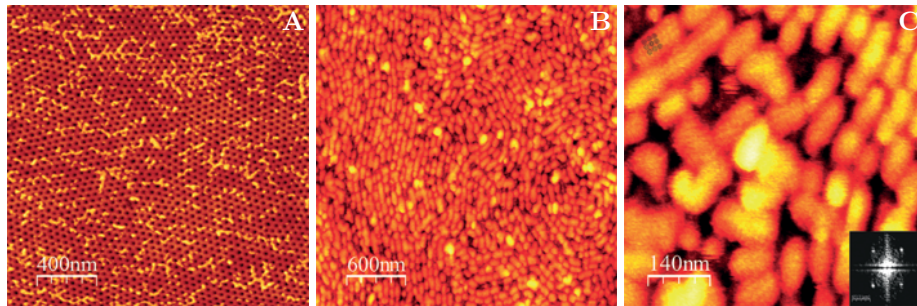


Figure A.1: SbpA self-assembly into confined S-layers on a block-copolymer substrate consisting of PolyStyrene (PS) and PolyEthylene Oxide (PEO).

(A) Shows a hexagonal dotted pattern with the preferential S-layer formation on hydrophobic PEO. The BC pattern is exposed to $6 \mu\text{g/ml}$ SbpA for 75 minutes. Imaged by ex-situ AFM in contact mode, Bruker SNL-D probe – 0.06 N/m.

(B) Shows a lamellar pattern where the S-layer formation follows the underlying lines. The BC pattern is exposed to $50 \mu\text{g/ml}$ and imaged by ex-situ AFM in contact mode, Bruker SNL-D probe – 0.06 N/m.

(C) Shows that the internal crystalline (inset) structure of the S-layer patches lines up with the line pattern underneath.

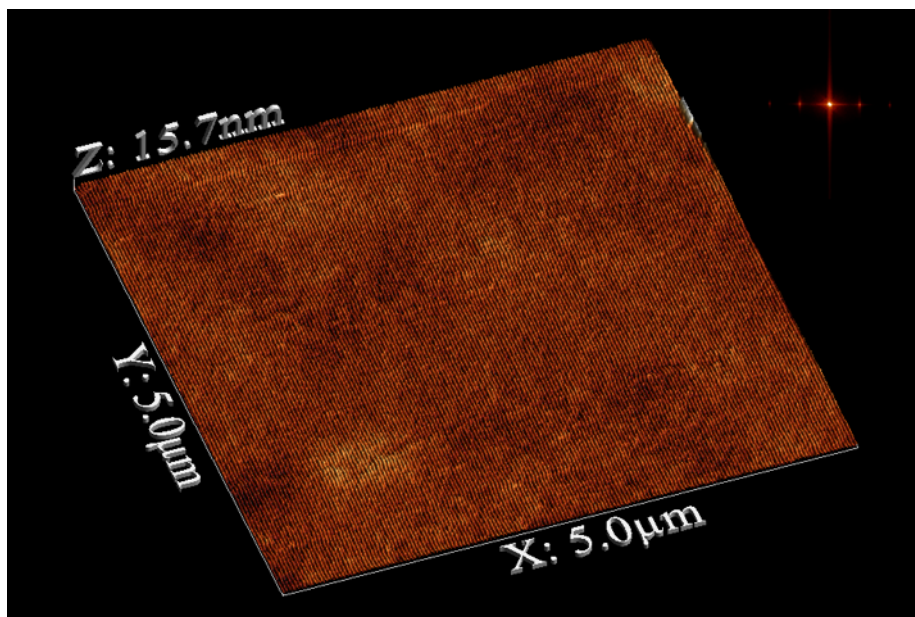


Figure A.2: A parallel line pattern of block-copolymer on an underlying sapphire substrate. Long range order without defects can be achieved. The lines are spaced exactly 33.3 nm apart, as is also shown by the FFT spectrum in the upper right corner. Imaged by ex-situ AFM in PeakForce Tapping mode, Bruker ScanAsyst Air – 70 kHz, 0.4 N/m.

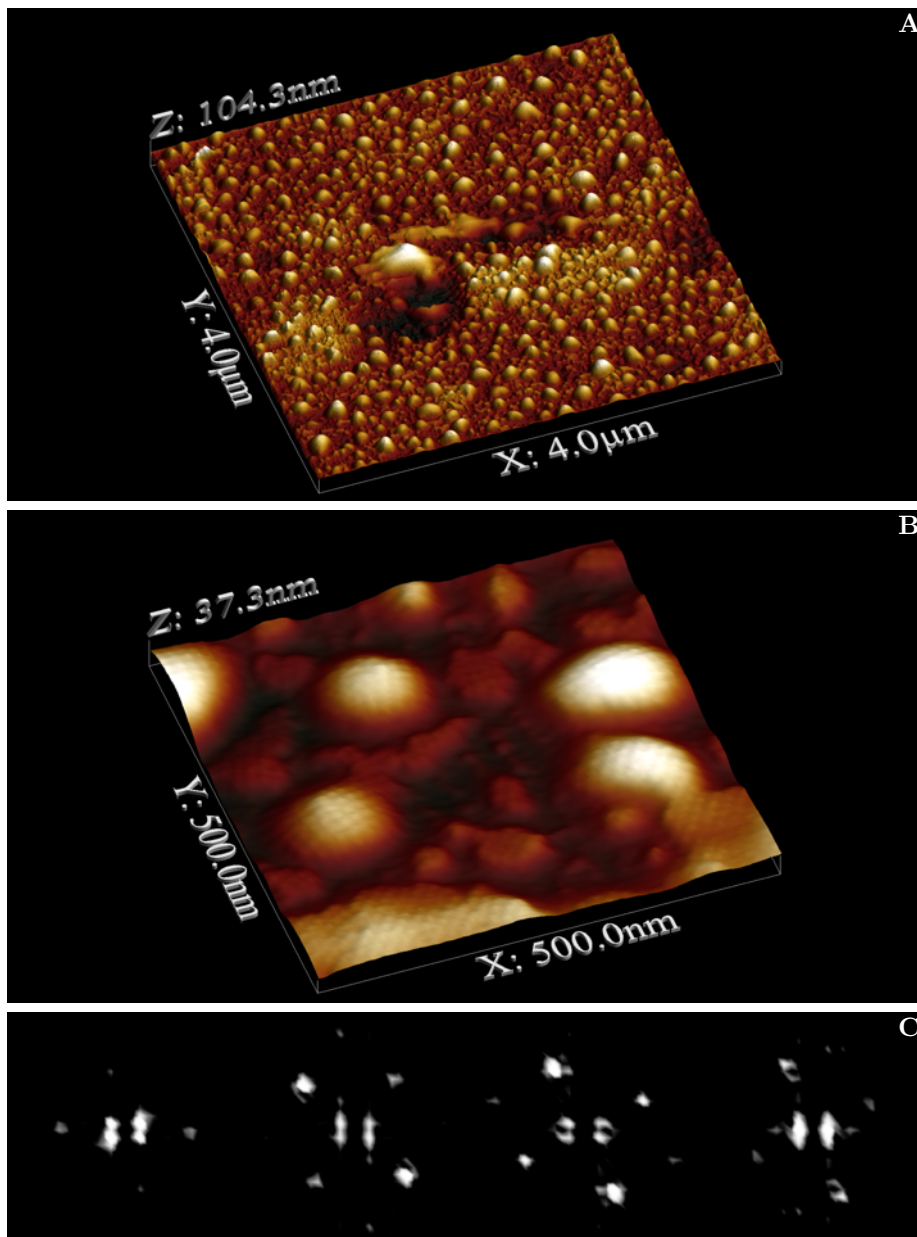


Figure A.3: A block copolymer surface as is also shown in figure A.2 is exposed to SbpA monomers overnight. The small planar patches correspond to S-layers directly deposited onto the underlying line pattern. The larger dome-shaped particles are S-layers covering small salt particles.

(A) An overview is shown where the underlying line pattern can be seen with the patches of S-layer scattered across. Imaged by in-situ AFM in TappingMode, Bruker FastScan-DX – 110 kHz, 0.25 N/m.

(B) A zoom clearly shows the typical crystalline fingerprint of S-layers on both the larger dome-shaped features as well as the smaller planar patches in between.

(C) FFT spectra are taken from four dome-shaped features in (A). The orientation of the FFT pattern reflects the random orientation of the S-layers.

B. Decomposition of ACC under influence of X-ray irradiation

Samples of Amorphous Calcium Carbonate (ACC) and Dehydrated Amorphous Calcium Carbonate (DACC) have been provided by Dr. Alejandro Fernandez-Martinez as part of our synchrotron beamtime at the ALS in September 2012. Their respective X-ray absorption spectra are shown in figures B.2 and B.3.

Changing X-ray absorption spectra during measurements

During XAS measurements these samples have been found to undergo a transformation. The initial spectrum in figure B.2 corresponds with literature values of ACC as are shown in figure B.1 in red and the initial spectrum in figure B.3 is similar to what is expected from dehydrated ACC as is shown in figure B.1 in green. Politi et. al studied the transformation from ACC to calcite and have found an intermediate form which can be identified by a single crystal field peak, no shoulder, at position b_1 . This spectrum is ascribed to dehydrated or anhydrous ACC [23, 24]. To the best of our knowledge this is the first time that synthetically prepared dehydrated ACC is measured. After ~ 90 minutes of X-ray irradiation, both spectra have undergone some significant changes resulting in the emergence of two pronounced satellite peaks.

When figure B.2 is compared to B.3 it seems that the transformation is further along in B.3 than it is in B.2. At the same time there is no change observed in the ACC spectrum between measurement 5 and 7.

This could indicate that only part of the sample area that is probed by the X-ray beam is transforming.

The reference spectra of calcite is compared to the absorption spectra of DACC. It is clear that the final state of DACC (DACCf) does not correspond with calcite, the peak position of the crystal field peaks is shifted to lower energies.

Decomposition of ACC and DACC under influence of X-ray radiation

The peak positions of DACCf are compared with peak positions of both calcite and calcium oxide in table B.1. The peak position and overall shape of the spectrum point to the fact that DACCf more closely resembles CaO than it does to calcite.

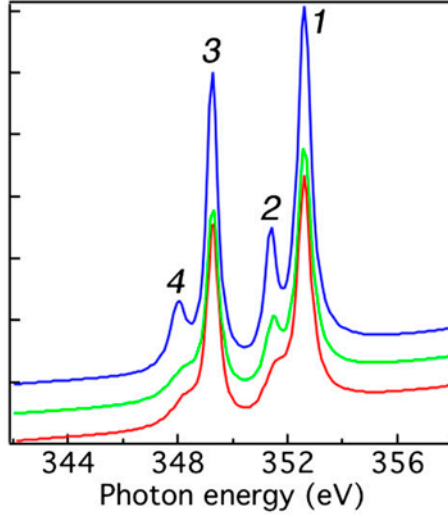


Figure B.1: Peak-fitted spectra of hydrated amorphous calcium carbonate ($\text{ACC} \cdot \text{H}_2\text{O}$) in red, in green anhydrous ACC and in blue crystalline calcite as identified by Politi et al. (Figure 1 from Gong et al. [24, 23]).

Material	b_2-b_1 (eV)	b_2-a_2 (eV)
Calcite	1.25	3.25
DACC (final state)	1.55	3.31
CaO	1.53	3.40

Table B.1: The energy differences between the second main peak and its satellite peak (b_2-b_1) and between the two main peaks (b_2-a_2) is given for calcite, calcium oxide and DACCf (figure B.3, measurement 5). Calcium oxide data by Miedema et al. [57].



Equation B.1: The thermal decomposition of calcium carbonate into calcium oxide and carbon dioxide [73].

Therefore it is assumed that exposure to X-ray radiation triggers the decomposition of amorphous CaCO_3 into CaO and CO_2 , equation B.1.

The transformation of calcium carbonate into calcium oxide – lime – at temperatures of 500-600 °C is well known reaction and is currently the most common method of manufacturing lime [73, 74]. XAS measurements on calcite showed no indication of decomposition. However transformation of CaCO_3 powder into CaO powder at temperatures as low as 100 °C has been reported [75].

This points to the possibility that the high energetic X-ray radiation in combination with UHV conditions can lower the reaction barrier, enabling the transformation of amorphous CaCO_3 into CaO under vacuum conditions at room temperatures and in the absence of S-layers.

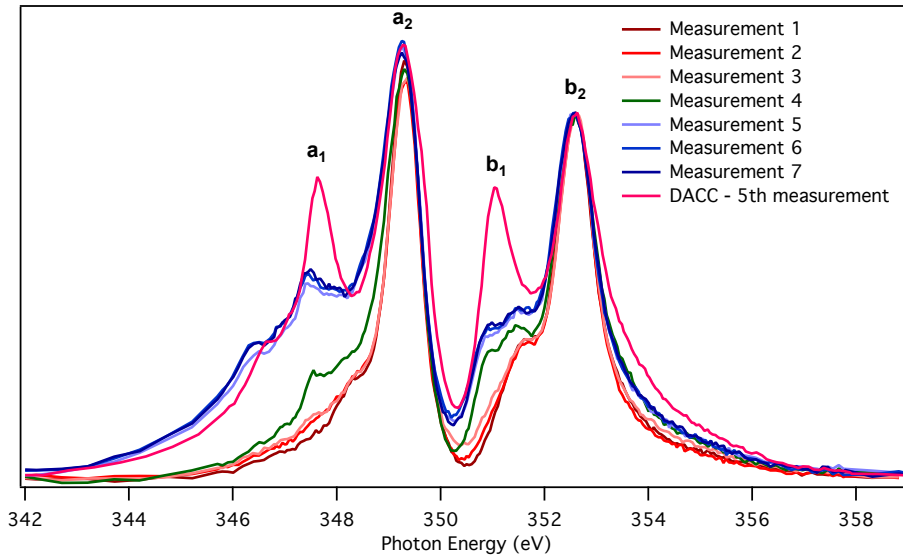


Figure B.2: The X-ray absorption spectrum of synthetically prepared amorphous calcium carbonate. The consecutive spectra show a transformation during measurements. A single spectrum takes about 14 minutes, making the total time between first and last measurement about 90 minutes. For comparison the last measurement from figure B.3 is included.

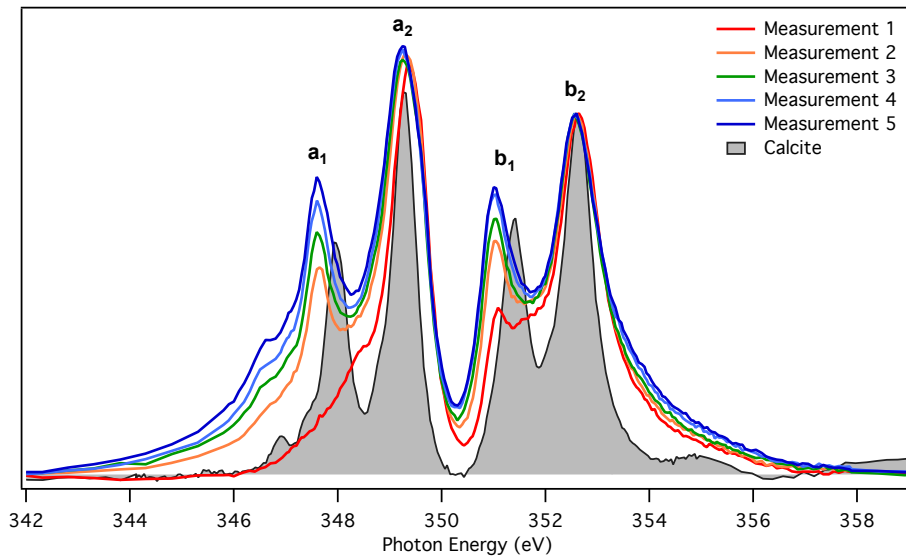


Figure B.3: The X-ray absorption spectrum of synthetically prepared dehydrated amorphous calcium carbonate. The consecutive spectra show a transformation during measurements. A single spectrum takes about 14 minutes, making the total time between first and last measurement about 70 minutes. For comparison the reference spectrum of calcite is included.

C. SbpA purification and S-layer growth protocols

The individual SbpA proteins can be purified by exposing S-layers to high concentrations of chaotropic agents, recrystallization can then occur through addition of Ca^{2+} .

Here I will give the protocols for ex-vivo S-layer crystallization and SbpA purification as designed by Norville et al. [45] and obtained from Dr. Seong-Ho Shin and Dr. Behzad Rad [16].

C.1 SbpA purification

The growth of a cell culture of *Lysinibacillus sphaericus* is a two step process. First a 20 ml seed solution is prepared which is then expanded to a 500 ml volume. After this the the cell wall is purified.

Cell growth

1.) Preparation of the growth solution (SVIII)

- SVIII ingredients:
 - 10 g/l peptone
 - 5 g/l meat extract
 - 0.2 mM MgSO_4 – Mw=120.37, 12 mg for 0.5 l
 - 1.8 mM sucrose – Mw=342.3, 308 mg for 0.5 l
 - 7 mM K_2HPO_4 – Mw=174.2, 609.7 mg for 0.5 l
- Fill a ~2 l Erlenmeyer flask with 470 ml SVIII.
- Fill a 250 ml Erlenmeyer flask with 18.8 ml SVIII.
- Close off the Erlenmeyers with aluminum foil, then place both in an autoclave set to 121 °C for about 50 minutes.
- Leave to cool to room temperature for about 1.5 hours.

Simultaneously the solutions that are needed later in the protocol can be prepared:

- 17 mM glucose (Mw=180.16)
- 50 mM HEPES at pH 7.2

- 50 mM Tris, pH 7.2 (Keep the solution cold by placing it in an ice bath or refrigerator.)
- 10% Triton X-100 (*Thermo Scientific, # 28314*)
- 1 M HEPES at pH 7.2 (Use filter sterilization.) – A minimum of 26 ml for 500 ml final culture.
- 1.67 M glucose (Use filter sterilization.) – A minimum of 5.2 ml for 500 ml final culture.

2.) Preparation of the 20 ml seed solution.

Get the sterilized 250 ml Erlenmeyer with 18.8 ml SVIII from step C.1 and follow the steps below:

- Add 1.0 ml of 1 M HEPES at pH 7.2
- Add 0.20 ml of 1.67 M glucose
- Combine this solution with scrapings from a glycerol stock of *Lysinibacillus sphaericus*.
The glycerol stock has been prepared by growing Lysinibacillus sphaericus overnight (~16 hours) in SVIII medium and then taking 1 mL and adding 250 μ l of 80% glycerol. After a 1 hr inoculation period the glycerol stock is placed in -80 °C freezer.
- Close the Erlenmeyer with aluminum foil and place it in a 32 °C environment for about 16 hours.
- After a 16 hour period the culture has become cloudy.

3.) The 20 ml seed solution is expanded to a 500 ml culture.

Take the ~2 l Erlenmeyer flask with 470 ml SVIII from 1 and follow the steps below:

- Add 25 ml of 1 M HEPES at pH 7.2
- Add 5 ml of 1.67 M glucose
- Leave for about 6-7 hours at 32 °C until it reaches an optical density (OD₆₀₀) of ~0.7-1.0. (The important aspect is that the growth medium has become cloudy due to bacteria growth.)
- Centrifuge the solution at 15.000 \times g at 4 °C for 20 minutes. (*Beckman JLA 8.1 Fixed-angle Rotor.*)
- Re-suspend each pellet in 30 ml solution containing 50 mM Tris at pH 7.2 and transfer it to an Oakridge Tube.
- Centrifuge the resulting solution at 16.000 \times g at 4 °C for 15 minutes. (*Beckman Coulter JA-20 Fixed-Angle Rotor*)
- Measure the weight of the wet cell pellet and discard the supernatant.
- When the cell wall purification is postponed to a later time, store the cell pellet at -80 °C.

Protein purification

1.) Lysing of cells.

First re-suspend the cell pellets in 28 ml of 50 mM Tris at pH 7.2 which is kept cold. (28 ml will work for up to 8 g of cell material, for more than 8 g add the buffer in a ratio of 100 g cell material to 350 ml buffer)

Lyse the suspended cells in ice by sonicating with 2 s pulses and 2 s pauses at an output power ~ 21 W. (corresponding to power level 7 for a Misonix sonicator 3000.) Repeat this procedure three times with a 1 minute cooling period between each cycle.

A alternative and preferred Lysis method uses the EmulsiFlex-C3 homogenizer from Avestin. The cells are passed 3 times through the system at a pressure of 20.000 psi and with a cooling loop through an ice bath.

When Lysed, centrifuge the cells at $28.000 \times g$ at 4°C for 15 minutes. (*Beckman Coulter JA-20 Fixed-Angle Rotor*)

2.) Purification of cell wall.

- Use a disposable plastic spatula to separate the cell wall (the white outer ring of the pellet) from the unbroken cells (the tan inner ring).
- Add 18 ml of Tris at pH 7.2
- Sonicate the solution in an ice bath for ~ 1 minute with 1 second pulses separated by 1 second pauses.
- Add 1.8 ml of 10% Triton X-100
- Stir the solution for 10 minutes at room temperature at 300 rpm (The suspension is initially pale pink and becomes white cloudy as it is washed).
- Spin the suspension at $40.000 \times g$ for 10 minutes at 4°C . (*Beckman Coulter JA-20 Fixed-Angle Rotor*)

This purification procedure is repeated four to five times, see also figure C.2. The final pellet is the purified cell wall and can be store at -20°C until the next step.

3.) Denaturing of purified cell wall.

- The pellet containing the purified cell walls is dissolved in 10 mL of 50 mM Tris at pH 7.2 and 5M guanidium chloride (GHC1). This is then incubated for 30 minutes at room temperature while slowly shaking.
- The resulting solution is centrifuged at $100.000 \times g$ at 4°C for 45 minutes. (*SW28Ti rotor, Beckman coulter, Optima L-100XP*)
- The supernatant is decanted and dialyzed against 2 l of deionized water at 4°C for 2 hours. Place the dialysis tube into 2 l fresh deionized water after every 40 minutes.
- The final solution (~ 12 ml) is centrifuged again at $100.000 \times g$ at 4°C for 30 minutes.

$$A = \epsilon c l \quad (\text{C.1})$$

$$\epsilon_{280} = 0.5978(\text{mg/ml})^{-1}\text{cm}^{-1} \quad (\text{C.2})$$

Equations C.1 and C.2: Beer's law (C.1) relates the absorption (A) to the concentration (c) and optical path length (l) through the absorption coefficient (ϵ) [76]. For SbpA proteins from the *Lysinibacillus sphaericus* the absorption coefficient at a wavelength of 280 nm (ϵ_{280}) is known and can be used to determine the concentration by measuring the absorption and optical path length.

4.) Measuring the concentration.

The concentration is determined using a visible light absorption measurement as is shown in figure C.1. The concentration of SbpA is then calculated using Beer's law and the absorption coefficient for SbpA at a wavelength of 280 nm, equations C.1 and C.2 [76].

By following this protocol usually a concentration of 1.5 ~ 2.0 mg/ml is obtained.

In order to reduce aggregation and for consistency the concentration is adjusted to ~ 1.5 mg/ml

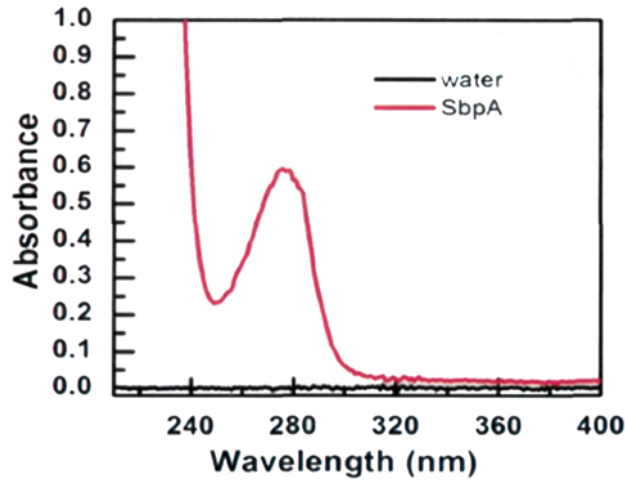


Figure C.1: The absorbance of a solution containing SbpA proteins and a reference solution containing deionized water. The absorbance of water is set to zero so that the absorbance of the solution containing SbpA only depends on the protein concentration. Equations C.1 and C.2 can be used to determine the concentration of SbpA. The SbpA protein has a strong absorption around 280 nm, contaminants like DNA or aggregates have absorption peaks around 260 nm and 340 nm respectively. $A_{260}/A_{280} = 0.6$ indicates very little DNA contamination, $A_{340}/A_{280} < 0.05$ indicates little scattering and therefore few aggregates.

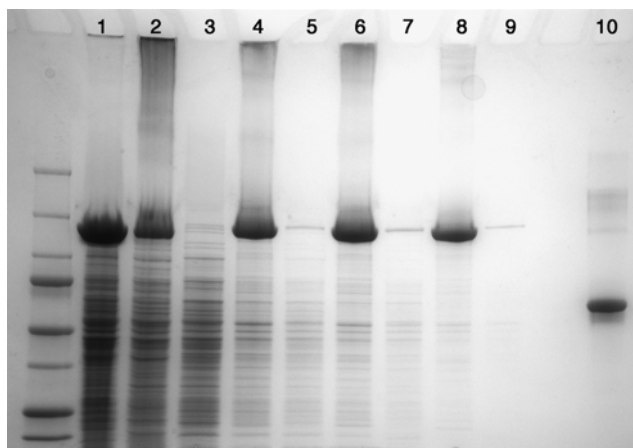


Figure C.2: Gel electrophoresis taken at different steps in the SbpA protocol. 1.) The crude cell lysate. 2.) The first wash before centrifugation. 3.) The first supernatant. 4.) The second wash before centrifugation. 5.) The second supernatant. 6.) The third wash before centrifugation. 7.) The third supernatant. 8.) The final wash before centrifugation. 9.) The final supernatant. 10.) 5 μg BSA (Bovine Serum Albumin) reference. It is clear that after four washes, the supernatant contains few contaminants, indicating that the cell wall is sufficiently purified.

C.2 Ex-vivo S-layer crystallization

S-layers can be recrystallized ex-vivo from previously purified SbpA monomers. Based on the concentration of SbpA used in this procedure, the S-layers either form immobilized on the surface or also free floating in solution.

For immobilized S-layers the following protocol is used, based on in-situ AFM S-layer measurements by Chung et al. [16].

- Prepare SbpA at a concentration of 50 $\mu\text{g}/\text{ml}$ in a buffer solution containing:
 - 50 mM CaCl_2
 - 100 mM NaCl_2
 - 10 mM Tris at pH 7.2
- A drop is placed on the sample surface and left to incubate for ~ 5 hours. *When a mica substrate is used, it is preferred to use an incubation time of at least 10 hours. This in order to allow the monocrystalline S-layer domains to relax to a thermodynamically stable state. See also paragraph 3.1 [12].*
- To remove excess SbpA protein and possible S-layers that have formed in solution, the drop on the surface is replaced by deionized water for several times.

In some instances a higher concentration of S-layers is required. This can be achieved by crystallizing S-layers free floating in solution and subsequently centrifuging them to a pellet, which can be dissolved in a smaller volume to increase the concentration.

- Prepare SbpA at a concentration of up to 1 mg/ml in a buffer solution containing:
 - 50 mM CaCl_2
 - 100 mM NaCl_2
 - 10 mM Tris at pH 7.2
- Let the solution incubate overnight, the solution will turn slightly opaque during S-layer crystallization.
- Centrifuge the resulting solution at $20.000 \times g$ for 10 minutes. (*General eppendorf tabletop centrifuge.*)
- Discard the supernatant and redissolve the S-layer to obtain the desired concentration.

D. Data analysis of X-ray Absorption spectra

The analysis method that is used is based on the analysis of Politi et. al of similar X-ray absorption spectra. [23] The computer program Igor Pro and a dedicated analysis package is used to apply this method to the raw measurement data [77].

The X-ray absorption probability is measured by comparing the incoming X-ray intensity and the reflected intensity, I_0 and I_r respectively. The absorption probability is then simply calculated as $I=I_r/I_0$ and plotted as function of the X-ray energy, see figure D.1(A).

First the pre-edge is set to zero and the x-axis is shifted so that second main peak is set at 352.6 eV following Benzerara et al. and Politi et al., see figure D.1(B) [23, 52].

Second the ionization potentials are removed by fitting and subsequently subtracted two arc tangent functions. The spectrum is normalized by setting the intensity the L_{II} peak to 1, see equation D.1 and figure D.1(C) [78].

$$I = A \left(\frac{3\pi}{4} + \arctan \left(\frac{x - x_{p1}}{\omega} \right) + \frac{1}{2} \cdot \arctan \left(\frac{x - x_{p2}}{\omega} \right) \right) \quad (D.1)$$

Equation D.1: Here I is the ionization energy of the calcium L_{II} and L_{III} edge, x_{p1} and x_{p2} are the energies of both main peaks and ω is the width and is set to 0.2 following presets from the Igor Pro XAS analysis package [77]. The value of A is set to the intensity of the post-edge, so that so that after subtraction of the ionization energy both pre-edge and post-edge are equal to zero.

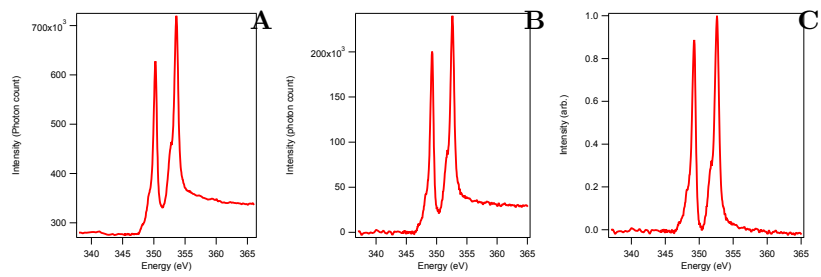


Figure D.1: A consecutive set of spectra with increasing amount of analysis applied.
 (A) The raw spectrum defined by $I=I_r/I_0$.
 (B) The pre-edge is set to zero and the energy values are calibrated so that the second main peak is set to 352.6 eV following Benzera et al. and Politi et al. [23, 52].
 (C) The background as is calculated in equation D.1 is subtracted so that both pre-edge and post-edge equal zero.

Bibliography

- [1] Intergovernmental Panel on Climate Change. IPCC press release: Human influence on climate clear, IPCC report says, 2013.
- [2] S. M. Benson and F. M. Orr. Carbon Dioxide Capture and Storage. *MRS Bulletin*, 33(4):303–305, 2008.
- [3] C. Jansson, S. D. Wullschleger, U. C. Kalluri, and G. A. Tuskan. Phytosequestration: Carbon Biosequestration by Plants and the Prospects of Genetic Engineering. *Bioscience*, 60(9):685–696, 2010.
- [4] J. W. Morse, F. J. Millero, V. Thurmond, E. Brown, and H. G. Ostlund. The carbonate chemistry of grand bahama bank waters - after 18 years another look. *Journal of Geophysical Research-Oceans*, 89(Nc3):3604–3614, 1984.
- [5] M. Obst, J. J. Dynes, J. R. Lawrence, G. D. W. Swerhone, K. Benzerara, C. Karunakaran, K. Kaznatcheev, T. Tyliczszak, and A. P. Hitchcock. Precipitation of amorphous CaCO_3 (aragonite-like) by cyanobacteria: A STXM study of the influence of EPS on the nucleation process. *Geochimica Et Cosmochimica Acta*, 73(14):4180–4198, 2009.
- [6] J. B. Thompson, S. SchultzeLam, T. J. Beveridge, and D. J. DesMarais. Whiting events: Biogenic origin due to the photosynthetic activity of cyanobacterial picoplankton. *Limnology and Oceanography*, 42(1):133–141, 1997.
- [7] S. Schultzelam and T. J. Beveridge. Nucleation of celestite and strontianite on a cyanobacterial s-layer. *Applied and Environmental Microbiology*, 60(2):447–453, 1994.
- [8] C. Jansson and T. Northen. Calcifying cyanobacteria – the potential of biomineralization for carbon capture and storage. *Current Opinion in Biotechnology*, 21(3):365–371, 2010.
- [9] Nina Kamennaya, Caroline Ajo-Franklin, Trent Northen, and Christer Jansson. Cyanobacteria as Biocatalysts for Carbonate Mineralization. *Minerals*, 2(4):338–364, 2012.
- [10] H. Engelhardt. Are S-layers exoskeletons? the basic function of protein surface layers revisited. *Journal of Structural Biology*, 160(2):115–124, 2007.

- [11] T. Pavkov-Keller, S. Howorka, and W. Keller. The Structure of Bacterial S-Layer Proteins. *Molecular Assembly in Natural and Engineered Systems*, 103:73–130, 2011.
- [12] S. H. Shin, S. Chung, B. Sanii, L. R. Comolli, C. R. Bertozzi, and J. J. De Yoreo. Direct observation of kinetic traps associated with structural transformations leading to multiple pathways of s-layer assembly. *Proceedings of the National Academy of Sciences of the United States of America*, 109(32):12968–12973, 2012.
- [13] D. Pum and U. B. Sleytr. The application of bacterial s-layers in molecular nanotechnology. *Trends in Biotechnology*, 17(1):8–12, 1999.
- [14] Jenny A. Cappuccio, Gillian V. Lui, Veronica D. Pillar, and Caroline M. Ajo-Franklin. Tuning Microbial Surfaces to Control Carbonate Mineralization. *Biophysical Journal*, 102(3, Supplement 1):188a, 2012.
- [15] U. B. Sleytr, E. M. Egelseer, N. Ilk, D. Pum, and B. Schuster. S-layers as a basic building block in a molecular construction kit. *Febs Journal*, 274(2):323–334, 2007.
- [16] S. Chung, S. H. Shin, C. R. Bertozzi, and J. J. De Yoreo. Self-catalyzed growth of S layers via an amorphous-to-crystalline transition limited by folding kinetics. *Proceedings of the National Academy of Sciences of the United States of America*, 107(38):16536–16541, 2010.
- [17] U. B. Sleytr, P. Messner, D. Pum, and M. Sara. Crystalline bacterial cell Surface layers (S layers): From supramolecular cell structure to biomimetics and nanotechnology. *Angewandte Chemie-International Edition*, 38(8):1035–1054, 1999.
- [18] J. J. De Yoreo and P. G. Vekilov. Principles of Crystal Nucleation and Growth. *Biomineralization*, 54:57–93, 2003.
- [19] Q. Hu, M. H. Nielsen, C. L. Freeman, L. M. Hamm, J. Tao, J. R. I. Lee, T. Y. J. Han, U. Becker, J. H. Harding, P. M. Dove, and J. J. De Yoreo. The thermodynamics of calcite nucleation at organic interfaces: Classical vs. non-classical pathways. *Faraday Discussions*, 159:509–523, 2012.
- [20] D. Gebauer, A. Volkel, and H. Colfen. Stable Prenucleation Calcium Carbonate Clusters. *Science*, 322(5909):1819–1822, 2008.
- [21] E. M. Pouget, P. H. H. Bomans, J. A. C. M. Goos, P. M. Frederik, G. de With, and N. A. J. M. Sommerdijk. The Initial Stages of Template-Controlled CaCO₃ Formation Revealed by Cryo-TEM. *Science*, 323(5920):1455–1458, 2009.
- [22] Adam F. Wallace, Lester O. Hedges, Alejandro Fernandez-Martinez, Paolo Raiteri, Julian D. Gale, Glenn A. Waychunas, Stephen Whitelam, Jillian F. Banfield, and James J. De Yoreo. Microscopic Evidence for Liquid-Liquid Separation in Supersaturated CaCO₃ Solutions. *Science*, 341(6148):885–889, 2013.

- [23] Y. Politi, R. A. Metzler, M. Abrecht, B. Gilbert, F. H. Wilt, I. Sagi, L. Addadi, S. Weiner, and P. U. P. A. Gilbert. Transformation mechanism of amorphous calcium carbonate into calcite in the sea urchin larval spicule (vol 105, pg 17362, 2008). *Proceedings of the National Academy of Sciences of the United States of America*, 105(50):20045–20045, 2008.
- [24] Y. U. T. Gong, C. E. Killian, I. C. Olson, N. P. Appathurai, A. L. Amasino, M. C. Martin, L. J. Holt, F. H. Wilt, and P. U. P. A. Gilbert. Phase transitions in biogenic amorphous calcium carbonate. *Proceedings of the National Academy of Sciences of the United States of America*, 109(16):6088–6093, 2012.
- [25] Z. N. Zhang, Y. D. Xie, X. R. Xu, H. H. Pan, and R. K. Tang. Transformation of amorphous calcium carbonate into aragonite. *Journal of Crystal Growth*, 343(1):62–67, 2012.
- [26] Pradyot Patnaik. *Handbook of inorganic chemicals*. McGraw-Hill handbooks. McGraw-Hill, New York, 2003.
- [27] G. Binnig, C. F. Quate, and C. Gerber. Atomic Force Microscope. *Physical Review Letters*, 56(9):930–933, 1986.
- [28] Bede Pittenger, Natalia Erina, and Chanmin Su. Quantitative Mechanical Property Mapping at the Nanoscale with PeakForce QNM. *Application Note Veeco Instruments Inc*, 2010.
- [29] D. Ziegler, T. R. Meyer, R. Farnham, C. Brune, A. L. Bertozzi, and P. D. Ashby. Improved accuracy and speed in scanning probe microscopy by image reconstruction from non-gridded position sensor data. *Nanotechnology*, 24(33), 2013.
- [30] J. E. Penner-Hahn. X-ray absorption spectroscopy in coordination chemistry. *Coordination Chemistry Reviews*, 192:1101–1123, 1999.
- [31] M. Newville. *Fundamentals of EXAFS*. Univeristy of Chicago, Chicago, 2004.
- [32] A. C. Thompson, D. T. Attwood, E. M. Gullikson, M. R. Howels, J. B. Kortright, A. L. Robinson, J. H. Underwood, K. J. Kim, J. Kirz, I. Lindau, P. Pianetta, H. Winick, G. P. Williams, and J. H. Scofield. *X-Ray Data Booklet*. Lawrence Berkeley National Laboratory, Berkeley, second edition edition, 2001.
- [33] Ernest O. Lawrence and M. Stanley Livingston. THE PRODUCTION OF HIGH SPEED LIGHT IONS WITHOUT THE USE OF HIGH VOLTAGES. *Physical Review*, 40(1):19–35, 1932.
- [34] J. E. Cunningham. Synchrotron-radiation research. Technical report, Oak Ridge National Laboratory, 1982.
- [35] J. Clerk Maxwell. A dynamical theory of the electromagnetic field. *Philosophical Transactions of the Royal Society of London*, 155:459–512, 1865.
- [36] A. Einstein. Zur Elektrodynamik bewegter Körper. *Annalen der Physik*, 322(10):891–921, 1905.

- [37] J. B. West and H. A. Padmore. *Handbook on Synchrotron Radiation 2*. Elsevier, Amsterdam, 1987.
- [38] Helmut Wiedemann. *Synchrotron radiation*. Advanced texts in physics., Springer, Berlin ; New York, 2003.
- [39] B. Beckhoff, B. Kanngiesser, N. Langhoff, R. Wedell, and H. Wolff. *Handbook of Practical X-Ray Fluorescence Analysis*. Springer, Berlin, 2006.
- [40] P. Auger. Sur les rayons β secondaires produits dans un gaz par des rayons X. *Comptes Rendus de l'Académie des Sciences*, 177:169, 1923.
- [41] G. W. Goodrich and W. C. Wiley. Continuous Channel Electron Multiplier. *Review of Scientific Instruments*, 33(7):761–762, 1962.
- [42] J. H. Guo, Y. Luo, A. Augustsson, S. Kashtanov, J. E. Rubensson, D. K. Shuh, H. Agren, and J. Nordgren. Molecular Structure of Alcohol-Water Mixtures. *Physical Review Letters*, 91(15), 2003.
- [43] H. J. Liu, J. H. Guo, Y. D. Yin, A. Augustsson, C. L. Dong, J. Nordgren, C. L. Chang, P. Alivisatos, G. Thornton, D. F. Ogletree, F. G. Requejo, F. de Groot, and M. Salmeron. Electronic structure of cobalt nanocrystals suspended in liquid. *Nano Letters*, 7(7):1919–1922, 2007.
- [44] Atomic Molecular Systems and Optical Database. Photon cross sections and attenuation coefficients, 2000.
- [45] J. E. Norville, D. F. Kelly, T. F. Knight, A. M. Belcher, and T. Walz. Fast and easy protocol for the purification of recombinant S-layer protein for synthetic biology applications. *Biotechnology Journal*, 6(7):807–811, 2011.
- [46] H. Engelhardt and J. Peters. Structural research on surface layers: A focus on stability, surface layer homology domains, and surface layer cell wall interactions. *Journal of Structural Biology*, 124(2-3):276–302, 1998.
- [47] E. S. Gyoryvary, O. Stein, D. Pum, and U. B. Sleytr. Self-assembly and recrystallization of bacterial s-layer proteins at silicon supports imaged in real time by atomic force microscopy. *Journal of Microscopy-Oxford*, 212:300–306, 2003.
- [48] S. Whitelam. Control of pathways and yields of protein crystallization through the interplay of nonspecific and specific attractions. *Physical Review Letters*, 105(8), 2010.
- [49] National Institute of Standards and Technology. Solubility database, 2013.
- [50] Lawrence Berkeley National Laboratory. Advanced Light Source: Beamline 8.0.1 Endstations, 2013.
- [51] S. J. Naftel, T. K. Sham, Y. M. Yiu, and B. W. Yates. Calcium L-edge XANES study of some calcium compounds. *Journal of Synchrotron Radiation*, 8:255–257, 2001.
- [52] K. Benzerara, T. H. Yoon, T. Tyliczszak, B. Constantz, A. M. Spormann, and G. E. Brown. Scanning transmission X-ray microscopy study of microbial calcification. *Geobiology*, 2(4):249–259, 2004.

- [53] J. Y. Peter Ko, Xing-Tai Zhou, Franziskus Heigl, Tom Regier, Robert Blyth, and Tsun-Kong Sham. X-Ray Absorption Near-Edge Structure (XANES) of Calcium $L_{3,2}$ Edges of Various Calcium Compounds and X-Ray Excited Optical Luminescence (XEOL) Studies of Luminescent Calcium Compounds. *AIP Conference Proceedings*, 882(1):538–540, 2007.
- [54] UC Davis CHEMWiki. X-ray Spectroscopy, 2013.
- [55] F. M. F. de Groot, J. C. Fuggle, B. T. Thole, and G. A. Sawatzky. $2p$ x-ray absorption of $3d$ transition-metal compounds: An atomic multiplet description including the crystal field. *Physical Review B*, 42(9):5459–5468, 1990.
- [56] F. de Groot. Multiplet effects in X-ray spectroscopy. *Coordination Chemistry Reviews*, 249(1-2):31–63, 2005.
- [57] P. S. Miedema, H. Ikeno, and F. M. F. de Groot. First principles multiplet calculations of the calcium $L_{2,3}$ x-ray absorption spectra of CaO and CaF₂. *Journal of Physics-Condensed Matter*, 23(14), 2011.
- [58] Z. Hu, H. von Lips, M. S. Golden, J. Fink, G. Kaindl, F. M. F. de Groot, S. Ebbinghaus, and A. Reller. Multiplet effects in the Ru $L_{2,3}$ x-ray-absorption spectra of Ru(IV) and Ru(V) compounds. *Physical Review B*, 61(8):5262–5266, 2000.
- [59] T. K. Sham and I. Coulthard. Edge-jump inversion in the Si $L_{3,2}$ -edge optical XAFS of porous silicon. *Journal of Synchrotron Radiation*, 6:215–216, 1999.
- [60] M. Lingenfelder, S. H. Shin, S. Chung, and J. J. De Yoreo. Unraveling Mechanisms of CO₂ Sequestration on Self Assembled Surface Layer Proteins. In *MRS Spring Meeting 2012*.
- [61] D. Ricci and P. C. Braga. Recognizing and avoiding artifacts in AFM imaging. *Methods in Molecular Biology*, 242:25–37, 2004.
- [62] J. R. I. Lee, T. Y. J. Han, T. M. Willey, D. Wang, R. W. Meulenberg, J. Nilsson, P. M. Dove, L. J. Terminello, T. van Buuren, and J. J. De Yoreo. Structural Development of Mercaptophenol Self-Assembled Monolayers and the Overlying Mineral Phase During Templated CaCO₃ Crystallization from a Transient Amorphous Film. *Journal of the American Chemical Society*, 129(34):10370–10381, 2007.
- [63] M. J. Fasolka and A. M. Mayes. Block copolymer thin films: Physics and applications. *Annual Review of Materials Research*, 31:323–355, 2001.
- [64] R. A. Segalman. Patterning with block copolymer thin films. *Materials Science & Engineering R-Reports*, 48(6):191–226, 2005.
- [65] J. N. L. Albert and T. H. Epps. Self-assembly of block copolymer thin films. *Materials Today*, 13(6):24–33, 2010.

- [66] S. W. Hong, J. Huh, X. D. Gu, D. H. Lee, W. H. Jo, S. Park, T. Xu, and T. P. Russell. Unidirectionally aligned line patterns driven by entropic effects on faceted surfaces. *Proceedings of the National Academy of Sciences of the United States of America*, 109(5):1402–1406, 2012.
- [67] J. C. Wittmann and P. Smith. Highly oriented thin-films of poly(tetrafluoroethylene) as a substrate for oriented growth of materials. *Nature*, 352(6334):414–417, 1991.
- [68] D. Fenwick, P. Smith, and J. C. Wittmann. Epitaxial and graphoepitaxial growth of materials on highly orientated ptfe substrates. *Journal of Materials Science*, 31(1):128–131, 1996.
- [69] C. Y. Yang, Y. Yang, and S. Hotta. Crystal structure and polymorphism of dimethyl-oligothiophenes crystallized epitaxially on highly oriented PTFE thin films. *Molecular Crystals and Liquid Crystals Science and Technology*, 270:113–122, 1995.
- [70] S. K. Yan and J. Petermann. A method for comparing the nucleation ability of ptfe, ipp and spp on pe. *Polymer Bulletin*, 43(1):75–80, 1999.
- [71] K. Tanabe and M. Shiojiri. Epitaxial growth of polycyclic aromatic dyes on oriented polyethylene films. *Dyes and Pigments*, 34(2):121–132, 1997.
- [72] H. Suzuki, K. Oiwa, A. Yamada, H. Sakakibara, H. Nakayama, and S. Mashiko. Linear arrangement of motor protein on a mechanically deposited fluoropolymer thin-film. *Japanese Journal of Applied Physics Part 1-Regular Papers Short Notes Review Papers*, 34(7B):3937–3941, 1995.
- [73] David R. Lide. CRC Handbook of Chemistry and Physics, Internet Version 2005, 2005.
- [74] T. Oates. *Lime and Limestone*, pages 1–53. John Wiley & Sons, Inc., 2010.
- [75] N. B. Singh and N. P. Singh. Formation of CaO from thermal decomposition of calcium carbonate in the presence of carboxylic acids. *Journal of Thermal Analysis and Calorimetry*, 89(1):159–162, 2007.
- [76] ThermoSpectronic. Basic uv-vis theory, concepts and applications.
- [77] Beamline 7.0.1.1. XMCDPanel: Igor scripts for loading and treating the new version of the XAS data files, 2013.
- [78] D. A. Outka and J. Stohr. Curve fitting analysis of near-edge core excitation spectra of free, adsorbed, and polymeric molecules. *Journal of Chemical Physics*, 88(6):3539–3554, 1988.